

# Clinopyroxene/melt trace-element-partitioning in sodic alkaline magmas

Charles Beard<sup>a,\*</sup>, Vincent van Hinsberg<sup>a</sup>, John Stix<sup>a</sup>, Max Wilke<sup>b,c</sup>

<sup>a</sup>*Earth and Planetary Sciences, McGill University, 3450 University Street, Montreal, Québec, H3A 0E8, Canada*

<sup>b</sup>*Institut für Erd- und Umweltwissenschaften, Universität Potsdam, Golm, Germany*

<sup>c</sup>*Chemie und Physik der Geomaterialien, Deutsches GeoForschungsZentrum GFZ, Potsdam, Germany*

---

## Abstract

Clinopyroxene is a key fractionating phase in alkaline magmatic systems, but its impact on metal-enrichment processes, and the formation of REE + HFSE mineralisation in particular, are not well understood. To constrain the control of clinopyroxene on REE + HFSE behaviour in sodic (per)alkaline magmas, a series of internally heated pressure vessel experiments was performed to determine clinopyroxene-melt element-partitioning systematics. Synthetic tephriphonolite to phonolite compositions were run  $\text{H}_2\text{O}$ -saturated at 650–825°C with oxygen fugacity buffered to  $\log f\text{O}_2 \approx \Delta\text{QFM} + 1$  or  $\log f\text{O}_2 \approx \Delta\text{QFM} + 5$ . Clinopyroxene-glass pairs from basanitic to phonolitic fall deposits from Tenerife, Canary Islands, were also measured to complement our experimentally derived data set.

The REE partition coefficients are 0.3–53, typically 2–6, with minima for high-aegirine clinopyroxene. Diopside-rich clinopyroxene ( $\text{Ae}_{5-25}$ ) prefer the

---

\*corresponding author

Email address: [charles.beard@mail.mcgill.ca](mailto:charles.beard@mail.mcgill.ca) (Charles Beard)

MREE and have high REE partition coefficients ( $D_{Eu}$  up to 53,  $D_{Sm}$  up to 47). As clinopyroxene become more Na- and less Ca-rich (Ae<sub>25–50</sub>), REE incorporation becomes less favourable, and both the M1 and M2 sites expand (to 0.79 Å and 1.12 Å), increasing  $D_{LREE}/D_{MREE}$ . Above Ae<sub>50</sub>, both M sites shrink slightly and HREE ( $V^I r_i \leq 0.9 \text{ \AA} \approx \text{Y}$ ) partition strongly onto the M1 site, consistent with a reduced charge penalty for REE  $\leftrightarrow \text{Fe}^{3+}$  substitution.

Our data, complemented with an extensive literature database, constrain a model that predicts trace-element-partition coefficients between clinopyroxene and silicate melt using only mineral major-element compositions, temperature and pressure as input. The model is calibrated for use over a wide compositional range and can be used to interrogate clinopyroxene from a variety of natural systems to determine the trace-element concentrations in their source melts, or to forward model the trace-element evolution of tholeiitic mafic to evolved peralkaline magmatic systems.

*Keywords:* rare earth elements, aegirine, experimental petrology, Canary Islands, phonolite, peralkaline

---

## **1. Introduction**

Sodic clinopyroxene appear to more readily incorporate REE than their calcic equivalents (Marks et al., 2004), but despite fractionation of these minerals, melts in evolved alkaline systems can attain high REE contents, even up to economic levels (Kogarko, 1990; Downes et al., 2005; Marks et al., 2011; Sjöqvist et al., 2013; Goodenough et al., 2016; Möller and Williams-Jones, 2016). Trace-element data may be used to model magmatic processes (Spera and Bohrson, 2001; Troll and Schmincke, 2002; Boudreau, 2004; Xu et al., 2010; Girnis et al., 2013; Mungall and Brenan, 2014), but their interpretation requires precise knowledge of mineral/liquid element-partition coefficients. The approach has been applied to studies of mafic systems and mantle melting processes (Niu, 2004; Workman and Hart, 2005; Foley et al., 2013; Coumans et al., 2016; Peters et al., 2017). However, poor constraints on element-partitioning behaviour in alkaline and peralkaline rocks thus far preclude widespread application in these systems.

Experimental investigations of element-partitioning behaviour in alkali-enriched systems are limited in terms of composition (Wood and Trigila, 2001; Huang et al., 2006), and none yet have explored peralkaline conditions where molar  $(\text{Na}+\text{K})/\text{Al}$  exceeds 1. Additional information has been obtained from natural samples by measuring the concentration ratios of phenocryst–glass pairs from volcanic and intrusive rocks (Larsen, 1979; Wörner et al., 1983; Shearer and Larsen, 1994; Severs et al., 2009; Fedele et al., 2009; Mollo et al., 2016). However, these results may be biased by the presence of melt inclusions, mineral inclusions and mineral zoning, and their interpretation is commonly complicated by unknown or poorly constrained P-T-H<sub>2</sub>O-*f*O<sub>2</sub> con-

<sup>26</sup> ditions of equilibration and assumptions of closed-system behaviour.

<sup>27</sup> In this contribution, we present trace-element-partition coefficients be-  
<sup>28</sup> tween sodic clinopyroxene and silicate melts of tephriphonolite to phonolite  
<sup>29</sup> composition, as determined from internally heated pressure vessel experi-  
<sup>30</sup> ments on synthetic and natural compositions. These are complemented by  
<sup>31</sup> well-constrained natural volcanic phenocryst-glass pairs from Canary Islands  
<sup>32</sup> pyroclastic fall deposits. We characterise the mineral compositional controls  
<sup>33</sup> on element-partitioning behaviour and present a predictive model for clinopy-  
<sup>34</sup> roxene/melt element-partitioning that can be used to generate clinopyrox-  
<sup>35</sup> ene/melt partition coefficients using only clinopyroxene major-element com-  
<sup>36</sup> positions (e.g., as measured by electron-microprobe). This approach permits  
<sup>37</sup> forward modelling of element budgets during differentiation processes in mag-  
<sup>38</sup> matic systems, including evolved sodic alkaline systems, as well as providing  
<sup>39</sup> a mineral-based tool that can be used to reconstruct parental melt composi-  
<sup>40</sup> tions from clinopyroxene compositions in natural rocks.

## <sup>41</sup> 2. Methodology

### <sup>42</sup> 2.1. Experiment starting materials

<sup>43</sup> Clinopyroxene were synthesised in sodic alkaline melts of varying com-  
<sup>44</sup> position to obtain a range of mineral compositions consistent with those in  
<sup>45</sup> natural systems. Starting glass compositions are given in Table 1 and Figure  
<sup>46</sup> S1. Synthetic glasses L1 and L5 were prepared from reagent-grade oxide and  
<sup>47</sup> carbonate powders, ground together in an agate mortar, decarbonated for  
<sup>48</sup> 6 hrs at 450°C, then homogenised in air for 3 hrs at 1400°C in a Pt cru-  
<sup>49</sup> cible. Repeated fusion and grinding in agate ensured chemical homogeneity

50 of the starting glasses, which was confirmed by electron-microprobe analyses  
51 of the final fused glass. Finely-ground Mud Tank zircon was added to the  
52 homogeneous major-element glasses as a source of Zr, Hf, Nb and Ta; the  
53 glasses were then fused for a further three hours at 1400°C. The remaining  
54 trace-elements were added as a cocktail of single element nitrate solutions  
55 (ICP-MS standards), dried onto the powdered glasses, then denitrified at  
56 450°C for 30 minutes. The synthetic basanite L1 and phonolite L5 were  
57 mixed in varying proportions to make the low alkali (L) series of starting  
58 glasses, while dried NaOH and KOH powders were added to make the mid-  
59 dle (M) and high (H) alkali starting glasses. Analyses of glass compositions  
60 L5 and H5, quenched from superliquidus conditions, confirm that Henry's  
61 law was respected (Supplement S1).

62 A well-mixed rock powder from the Nechalacho Layered Suite in Canada  
63 (Möller and Williams-Jones, 2016, Unit NLS-9, sample L09-194-405.5, al-  
64 ternative sample name VM 11-6) was used as experimental starting mate-  
65 rial for a more extreme peralkaline composition. This composition was not  
66 fused prior to loading into experiment capsules, so as to preserve the origi-  
67 nal volatile-element concentrations. An experiment using this material that  
68 was quenched from superliquidus conditions is homogeneous with respect to  
69 major-elements, as determined from electron-microprobe measurements.

70 *2.2. Experimental equipment and procedures*

71 In total, 36 partitioning experiments were conducted in a Harwood-type  
72 internally heated pressure vessel (IHPV) in the HP-GeoMatS laboratory at  
73 the German GeoForschungsZentrum (Table S1). Temperature was measured  
74 with Type-S thermocouples calibrated against the melting point of NaCl

<sup>75</sup> (Borchert et al., 2010, accuracy of  $\pm 5$  °C at 200 MPa). Argon gas was used  
<sup>76</sup> as the pressure medium, and pressure was measured with a strain gauge to  
<sup>77</sup> an accuracy of  $\pm 7$  MPa. During the experiments, pressure was controlled  
<sup>78</sup> automatically and held within  $\pm 5$  MPa of stated values.

<sup>79</sup> Oxygen fugacity was buffered to the intrinsic redox conditions of the  
<sup>80</sup> experimental setup, which corresponds to  $\log f\text{O}_2 \text{ ca. } \Delta\text{QFM} + 1$  in our  $\text{H}_2\text{O}$ -  
<sup>81</sup> saturated charges (see Chou, 1986; Berndt et al., 2002; Jugo et al., 2010). One  
<sup>82</sup> experiment using the Nechalacho Layered Suite composition was performed  
<sup>83</sup> in a double capsule with a haematite solid buffer, designed to increase  $f\text{O}_2$   
<sup>84</sup> and promote crystallisation of  $\text{Fe}^{3+}$ -rich clinopyroxene (Eugster and Wones,  
<sup>85</sup> 1962). This experiment ran at the Hm-Mt buffer, which corresponds to  
<sup>86</sup>  $\log f\text{O}_2 \approx \Delta\text{QFM} + 5$ , as confirmed by presence of both buffer minerals in  
<sup>87</sup> the outer capsule following quench. The experiments were designed to run  
<sup>88</sup> between the liquidus and solidus for each composition, which corresponds to  
<sup>89</sup> temperatures between 650 and 825°C, all at 200 MPa pressure (Table S1).

<sup>90</sup> Powdered starting glass and distilled, deionised water were welded inside  
<sup>91</sup> 3.0 or 3.5 mm outer diameter platinum capsules of 20–25 mm length (see Ta-  
<sup>92</sup> ble S1). To verify that capsules were sealed, they were heated to 110°C and  
<sup>93</sup> weighed before and after. The amount of water sealed inside the capsules  
<sup>94</sup> varied with temperature and composition and was kept in excess of satu-  
<sup>95</sup> ration (Carroll and Blank, 1997; Moore et al., 1998; Schmidt and Behrens,  
<sup>96</sup> 2008). Water saturation was confirmed post-run by puncturing capsules and  
<sup>97</sup> checking for water expulsion and mass loss on drying at 110°C.

<sup>98</sup> The capsules were loaded into the vessel, pressurised to 200 MPa, then  
<sup>99</sup> heated to superliquidus temperatures for at least 16 hrs (Table S1) to per-

mit homogenisation of trace-element concentrations, dissolution of water and equilibration of  $fO_2$  by exchange of  $H_2$  through the capsule wall (cf. Gaillard et al., 2002). Following homogenisation, temperature was lowered to run conditions. An initial set of experiments were cooled rapidly from homogenisation to run temperature at about 100°C/min. A second set of experiments were cooled to run temperature at 1°C/min to promote slow growth of crystals and to minimise the formation of compositional gradients in the melt. Vessel temperature was then cycled between run temperature and run temperature + 10°C to promote dissolution of small crystals at the expense of larger grains, and to promote crystal growth close to the run temperature. Element partitioning results are consistent among experiments of different cooling paths. In all experiments, run temperature was kept constant for at least 40 hrs to allow for chemical homogenisation of melt and growth of crystals via Ostwald ripening. Capsules were then quenched to room temperature.

To minimise the growth of groundmass crystals on cooling, a rapid-quench apparatus was used where possible (Table 2). We have not measured quench rates in this vessel, but the capsules probably cooled at rates of several hundred degrees Celcius per second (e.g. Berndt et al., 2002). For the rest of the experiments, quenching was achieved by cutting power to the furnace, which resulted in cooling to below the glass-transition temperature (< 350°C; Giordano et al., 2005) in less than 150 seconds.

### 2.3. Natural samples

Alkaline volcanism on Tenerife is associated with a weak thermal mantle plume that impinges upon thick, old, slow-moving oceanic lithosphere (Car-

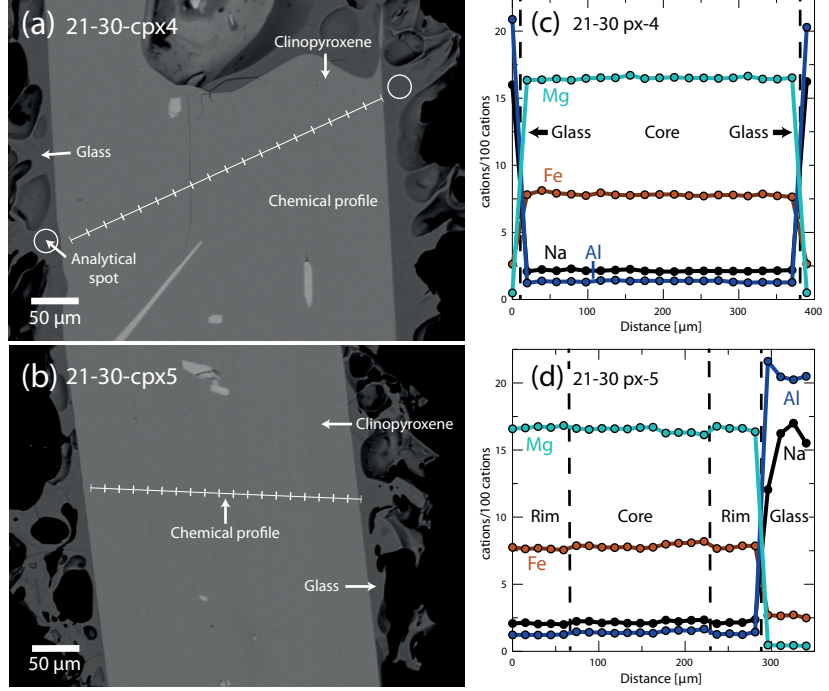


Figure 1: Examples of textural features from Canary Islands clinopyroxene phenocrysts from this study. (a, b) Backscattered electron images show that crystals are euhedral and are free from complex zoning patterns. (c, d) Chemical profiles across clinopyroxene phenocrysts and glass rims (quenched melt), as measured by wavelength dispersive spectroscopy, showing that zoning is effectively absent in these clinopyroxene. In (c) analyses of glass are aligned with the chemical profile shown in (a). Glass analyses shown in (d) are from rims of quenched melt from other clinopyroxene phenocrysts recovered from the same pumice sample. Both pictured phenocrysts are from the basal air fall deposit, associated with the  $\sim 2$  ka eruption of Pico Viejo, Tenerife (Ablay et al., 1995).

<sup>125</sup> racedo et al., 2007). This geological scenario has favoured development of a  
<sup>126</sup> complex magma-plumbing system that produces a great diversity of volcanic  
<sup>127</sup> products from alkali basalt to phonolite in composition. The Las Cañadas

<sup>128</sup> edifice, a large, central, composite stratovolcano (Bryan et al., 1998; Brown  
<sup>129</sup> et al., 2003; Edgar et al., 2007), rests upon a base of at least three mafic al-  
<sup>130</sup>kaline shield volcanoes (Thirlwall et al., 2000; Guillou et al., 2004; Gurenko  
<sup>131</sup>et al., 2006). Xenoliths indicate that a nepheline syenite intrusive system  
<sup>132</sup>underlies the island (Wiesmaier et al., 2012).

<sup>133</sup> Six clinopyroxene/glass pairs from four different volcanic eruptions on  
<sup>134</sup>Tenerife have been investigated. The  $\sim 2$  ka eruptive products of Montaña  
<sup>135</sup>Blanca and Pico Viejo (Abhay et al., 1995) are phonolitic, plinian fall de-  
<sup>136</sup>posits, whereas Montaña Samara is a monogenetic, mafic cinder cone (Albert  
<sup>137</sup>et al., 2015). Phase-equilibrium experiments conducted on Montaña Blanca  
<sup>138</sup>unit UMB-II suggest that magma was stored prior to eruption at  $850 \pm 15^\circ\text{C}$ ,  
<sup>139</sup> $50 \pm 20$  MPa, with  $2.5 \pm 0.5$  wt% H<sub>2</sub>O at  $\log f\text{O}_2 \approx \text{NNO} - 0.5$  (Andújar and  
<sup>140</sup>Scailet, 2012). Field locations, mineral proportions and major-element com-  
<sup>141</sup>positions of the clinopyroxene and glasses are presented in Table S1.

#### <sup>142</sup> 2.4. Sample preparation

<sup>143</sup> Experiment capsules were torn open with pliers, and charges were split  
<sup>144</sup>using a low-speed wafering saw. Samples were mounted in epoxy resin and  
<sup>145</sup>polished for *in-situ* chemical analyses.

<sup>146</sup> Natural pyroclastic rocks were rinsed in tap water and crushed with a  
<sup>147</sup>hammer. Crystals and glass fragments, hand-picked from a sieved size-  
<sup>148</sup>fraction between 1.18 mm and 125  $\mu\text{m}$ , were used to make grain mounts  
<sup>149</sup>containing 5–20 crystals of clinopyroxene per sample. Natural samples also  
<sup>150</sup>contain biotite, sanidine,  $\pm$  spinel, amphibole, olivine, titanite and sodalite.  
<sup>151</sup> Clinopyroxene mineral mounts were examined using backscattered electron  
<sup>152</sup>imaging to select euhedral crystals that were free from melt inclusions and

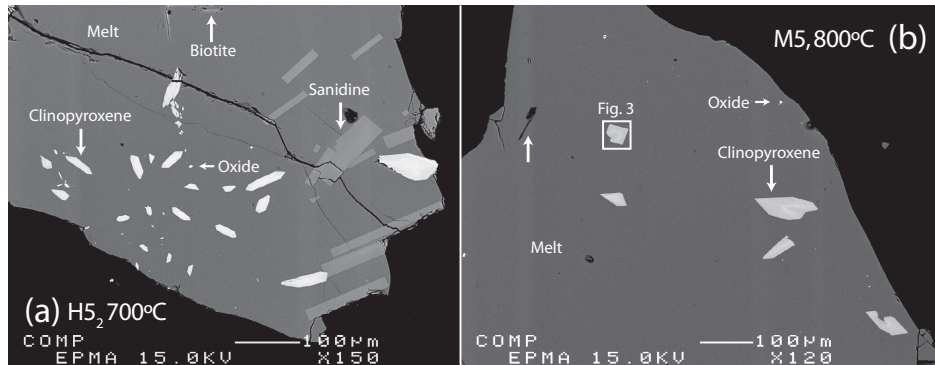


Figure 2: Backscattered electron images showing typical textures of run products from the internally heated pressure vessel experiments. Crystal fractions are typically small (<10% by area), with blade-shaped, euhedral clinopyroxene and glasses free of quench crystals.

<sub>153</sub> chemical zoning ( $n = 6$ , Fig. 1).

### <sub>154</sub> 3. Analytical techniques

<sub>155</sub> All experimental products were examined by reflected-light optical mi-  
<sub>156</sub> croscopy and scanning electron microscopy, and all phases produced were  
<sub>157</sub> identified by electron-microprobe using an energy-dispersive detector. Im-  
<sub>158</sub> ages were obtained to estimate modal proportions of phases, which were  
<sub>159</sub> calculated using ImageJ freeware (Rasband, 2016, see Table S1).

#### <sub>160</sub> 3.1. Electron-microprobe analysis

<sub>161</sub> Major-element compositions of experimental products and natural min-  
<sub>162</sub> erals and glasses were measured with a JEOL 8900 instrument at McGill  
<sub>163</sub> University and a JEOL 8230 instrument at the University of Ottawa (Table  
<sub>164</sub> 3). An accelerating voltage of 15 kV was used with a 15 nA beam of 5  $\mu\text{m}$   
<sub>165</sub> diameter for minerals, and a 4 nA beam of 50  $\mu\text{m}$  diameter for glasses. Count

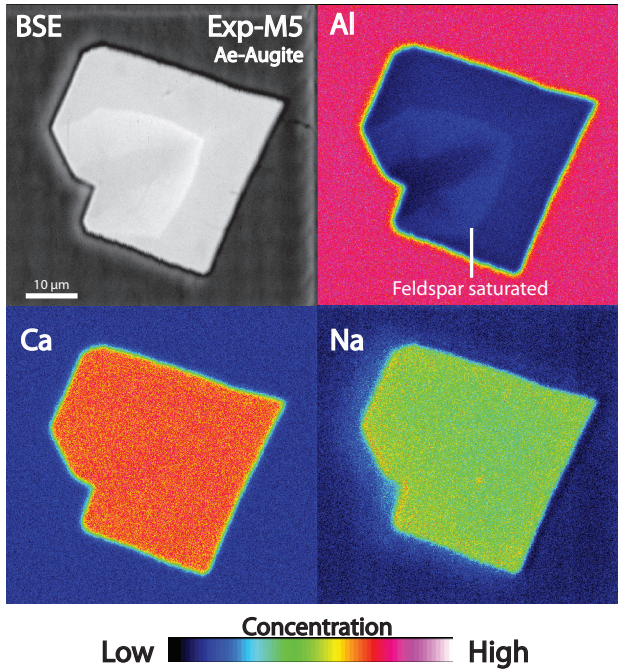


Figure 3: Element maps of clinopyroxene from internally heated pressure vessel experiment M5 (see box in lower magnification image, Fig. 2b). Aegirine-augite clinopyroxene have a sharp internal boundary that reflects feldspar saturation and are subtly zoned. Further element maps are available as an electronic supplement (Fig. S3).

times for all elements were 60 sec. Using the above routine, we observed no sodium loss over the measurement time period. For the silicate minerals and glasses, both synthetic and natural minerals or oxides were used for calibration (see Table S1). Analytical uncertainties were determined by multiple analyses of reference materials and duplicate analyses of samples.

Element distribution maps were generated with a JEOL 8900 instrument at McGill University using an accelerating voltage of 15 kV, a focussed 40 nA beam, and a dwell time of 50 ms per pixel (Figs. 3, S3). Fe, Ti, Al, Si

<sup>174</sup> and Na were measured with wavelength-dispersive detectors, while Ca and  
<sup>175</sup> Mg were measured with an energy-dispersive spectrometer.

<sup>176</sup> Transects of Ce, Mg and Fe concentrations within the experiment clinopy-  
<sup>177</sup> roxene were measured with a JEOL 8900 instrument at McGill University  
<sup>178</sup> using a focussed beam of 50 nA with an accelerating voltage of 20 kV. Ce was  
<sup>179</sup> counted with a wavelength-dispersive spectrometer with an LIFH crystal for  
<sup>180</sup> 100 sec (MAC-Ce standard). Mg and Fe were counted for 20 sec, with TAP  
<sup>181</sup> and LIF crystals respectively (diopside and olivine standards, respectively).  
<sup>182</sup> Matrix corrections for Mg, Fe and Ce were not possible with these data, for  
<sup>183</sup> lack of other major-elements measured, however their relative values may  
<sup>184</sup> still be used to assess the extent to which the clinopyroxene are chemically  
<sup>185</sup> zoned.

<sup>186</sup> *3.2. Laser-ablation ICP-MS*

<sup>187</sup> Trace-element concentrations of clinopyroxene and glasses were deter-  
<sup>188</sup> mined by laser-ablation ICP mass-spectrometry. Analyses were performed  
<sup>189</sup> at McGill University using a NewWave 213 nm Nd-YAG laser system coupled  
<sup>190</sup> to a Thermo Finnigan iCAP-Qc quadrupole ICP-MS instrument. Typical flu-  
<sup>191</sup> ence was 3–12 J/cm<sup>2</sup> (from 80 µm to 8 µm spot sizes), with a repetition rate  
<sup>192</sup> of 10 Hz. Ablated material was transferred to the ICP-MS in a He flow of 800  
<sup>193</sup> mL/min and mixed with Ar prior to injection into the plasma. Instrumental  
<sup>194</sup> drift was monitored by repeat analyses of the primary standard glass BCR-  
<sup>195</sup> 2G, with bias monitored by repeat analyses of secondary standards UTR-2  
<sup>196</sup> peralkaline rhyolite and USGS-RGM-1 rhyolite glasses (Table S1). Sample  
<sup>197</sup> surfaces were pre-ablated to remove residues from polishing materials and to  
<sup>198</sup> improve ablation efficiency.

199 Primary and secondary standards and an unzoned Canary Islands clinopy-  
200 roxene were analysed with beam sizes of 8–80  $\mu\text{m}$  to monitor crater-size-  
201 dependent element-fractionation effects; none were found for the elements  
202 reported here. For minerals and glasses in the experimental charges, beam  
203 sizes of 8–40  $\mu\text{m}$  and 16–80  $\mu\text{m}$  were used, respectively. Depending on grain-  
204 size and availability, 5–14 mineral grains and 3–10 areas of glass were anal-  
205 ysed per charge. Natural clinopyroxene and rim glasses were analysed using  
206 a beam size of 12–80  $\mu\text{m}$  and 12–30  $\mu\text{m}$ , respectively. Wherever possible,  
207 ablation was performed along lines parallel to crystal rims (1–3  $\mu\text{m} / \text{sec}$ ).

208 Drift corrections and data reduction were conducted in Iolite v2.5 (Paton  
209 et al., 2011). The total of major-elements measured by LA-ICP-MS or, where  
210 available, the Al concentration from electron-microprobe analyses, was used  
211 as an internal standard (Table 3). For some experiments, ablation through  
212 the minerals was too rapid to generate a stable signal for data-reduction  
213 purposes. In these cases, a mixing model was applied to estimate the com-  
214 position of these clinopyroxene, similar to those applied by Rubatto and  
215 Hermann (2007); Yang et al. (2018)(see supplementary methods S5).

## 216 4. Results

### 217 4.1. Run product phase stability and crystallinity

218 Trace-element partition-coefficients are reported for eleven experimental  
219 charges. 25 additional experiments were rejected as their run temperatures  
220 were superliquidus or subsolidus, or because their growth textures were in-  
221 dicative of disequilibrium (e.g. Fig. S3). Phase proportions are provided in  
222 Table S1.

223 All reported experimental runs were near-liquidus (3–22% crystals, RL  
224 images) and are characterised by a homogeneous distribution of phases (Fig  
225 2), except for experiments H5<sub>3</sub> and NLS-9<sub>2-HM</sub>, in which sanidine crystals  
226 are concentrated at the centre. Glasses are clean, homogeneous and show a  
227 limited range of major- and trace-element compositions for each experiment  
228 (Fig. S1). Clinopyroxene crystals are generally small, euhedral blades with  
229 a narrow range of sizes for a given experiment (<10 µm to 100 µm in cross  
230 section, Figs. 2–3). In addition to clinopyroxene and glass, experiments on  
231 mafic to intermediate compositions produced magnetite, titanite ± kaersu-  
232 tite amphibole, whereas some phonolitic experiments produced biotite, alkali  
233 feldspar ± magnetite (Table S1).

234 Constraining the full phase equilibria of all of the investigated composi-  
235 tions was beyond the scope of this study. Run conditions and run products  
236 given in Supplement S1 provide insight into phase equilibria that might guide  
237 future studies. In our experiments it can be seen that clinopyroxene has a  
238 wide stability field across the investigated physicochemical conditions, with  
239 only a single starting composition generating amphibole in place of pyroxene  
240 (experiments L3 and L3<sub>2</sub>).

#### 241 4.2. Glass compositions

242 All run-product glasses are homogeneous across the length and breadth  
243 of the experiment capsules based on multiple electron-microprobe and laser-  
244 ablation ICP-MS analyses. Most major-element oxide compositions, as mea-  
245 sured by electron-microprobe, show relative standard deviations of < 5%  
246 within experiment capsules, with minor-elements oxides (concentration <  
247 1%) showing greater variability, most with standard deviations between 5

and 10 % relative. Trace-element-compositions of the glass, as measured by laser-ablation ICP-MS, typically show time-weighted relative standard deviations of 1 to 8% within each capsule, with this variability depending on both the absolute concentration of that element and on the beam-size that was used for analyses (Supplement S1). Low sum-totals of major-element oxide concentrations in the electron-microprobe analyses are a result of high dissolved-water contents in the quenched melt.

On a total-alkalies vs. silica diagram the experiment glasses are predominantly phonolitic in composition, though span the trachyte-phonolite join (Fig. S1). Their alkalinity index (molar  $(\text{Na} + \text{K})/\text{Al}$ ) is 0.85 to 1.40, crossing the alkaline–peralkaline join, and the Mg# of these quenched melts is 0 (Mg-free) to 22. The dissolved water content of these quenched melts is 8.8 to 10.7 wt.% (by difference method from EPMA data, with the Fe oxidation state assigned following Kress and Carmichael 1991) and their NBO/T ratios are 0.98 to 1.42 (Mysen et al., 1982, 1985). The halogen content of the synthetic experiments is nominally zero, whereas glasses from the Nechalacho Layered Suite composition experiments typically contain 0.1 % F and 0.02 % Cl by weight.

The Canary Islands glasses are trachytic to phonolitic (CHECK) and are alkaline to weakly peralkaline in composition (alkalinity index of 0.78 to 1.16) with Mg# of 8 to 39. Dissolved water content and NBO/T ratios are not reported for these glasses because of post-eruptive loss of volatiles. These Canary Islands glasses typically contain 0.2 % F and 0.4 % Cl by weight.

**To add: a more comprehensive figure showing glass compositions. This could be in the main text, or as a supplement. Added**

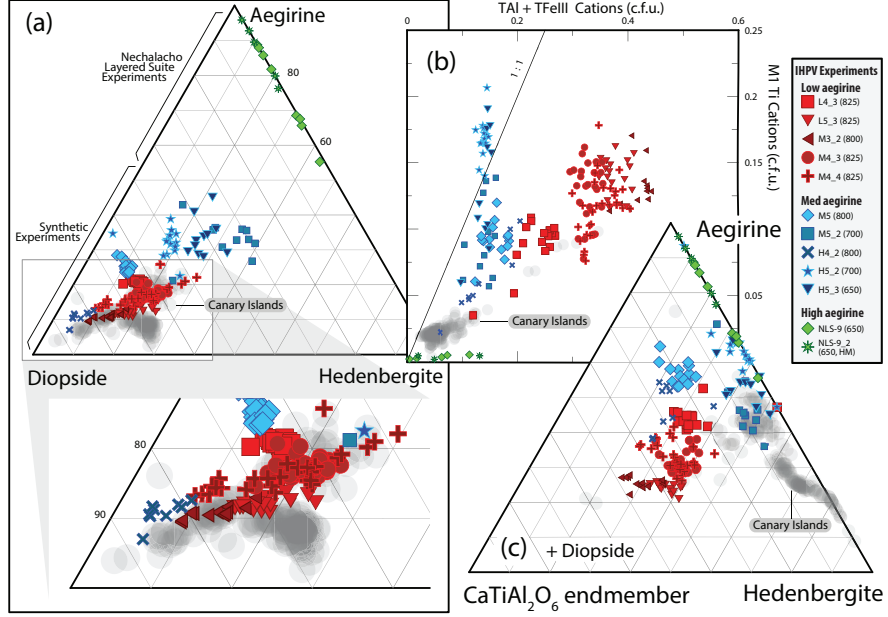


Figure 4: Clinopyroxene grown in internally heated pressure vessel experiments (a) expressed in terms of diopside, hedenbergite and aegirine end-members, (b) their M1Ti and tetrahedral Al and Fe<sup>3+</sup> contents, and (c) expressed in terms of aegirine, hedenbergite and the theoretical CaTiAl<sub>2</sub>O<sub>6</sub> end-member (Akasaka and Onuma, 1980). Clinopyroxene compositions from Canary Islands volcanic rocks are shown for comparison (this study). Fe<sup>2+</sup>/Fe<sup>3+</sup> within the clinopyroxene was assigned following Droop (1987), then site occupancies and end-member proportions were allocated following Morimoto (1989). For methods used in calculation of the end-member proportions see Supplement S5. The range of clinopyroxene compositions within each experiment records changes to the composition of the melt during crystal growth, whereby the cores of the crystals record the first stage of crystallisation and the rims (highest Fe, Na) are in equilibrium with the quenched melt. **to finish! Also re-plot with a separate symbol to signify Canaries compositions that were used for the derivation of partition coefficients**

<sup>273</sup> TAS, MgO vs. CaO and AI vs Mg#

274     *4.3. Compositions of the clinopyroxene and major-element exchange*

275     The Canary Islands clinopyroxene are diopside ( $\text{Di}_{60-90}$ ,  $\text{Ae}_{3-20}$  CHECK)  
276     in composition, with most crystals containing about 0.05 c.f.u.  ${}^{\text{IV}}\text{Al}$  (in the  
277     T site) and 0.02 c.f.u.  ${}^{\text{VI}}\text{Ti}$  (in the M1 site, Tables 3 and S1, Fig. 4). Ex-  
278     periments on the synthetic compositions produced clinopyroxene of diopside  
279     to aegirine-augite composition, a subset of which overlap with the compo-  
280     sitional space defined by the Canary Islands clinopyroxene on a diopside–  
281     hedenbergite–aegirine ternary diagram (Fig. 4a). This low-aegirine group  
282     of synthetic clinopyroxene display a positive correlation between  ${}^{\text{IV}}\text{Al}$  and  
283      ${}^{\text{VI}}\text{Ti}$  content (red, *low aegirine*,  $\text{Ae}_{5-25}$ ), and notably contain both of these  
284     elements at elevated concentration relative to the Canary Islands clinopy-  
285     roxene ( ${}^{\text{IV}}\text{Al} = 0.20\text{--}0.45$  c.f.u.,  ${}^{\text{VI}}\text{Ti} = 0.07\text{--}0.17$  c.f.u.). A further subset  
286     of synthetic clinopyroxene have higher aegirine content (blue, *med aegirine*,  
287      $\text{Ae}_{25-50}$ ) and show a similar range of Ti content to the low aegirine synthetic  
288     minerals (0.05–0.18 c.f.u.), but a limited range of lower  ${}^{\text{IV}}\text{Al}$  content (0.1–0.2  
289     c.f.u., Fig. 4b). Experiments performed on the Nechalacho Layered Suite  
290     composition (NLS-9, NLS-9<sub>2-HM</sub>, green, *high aegirine*,  $\text{Ae}_{55-95}$ ) reproduced  
291     the aegirine-augite to aegirine clinopyroxene from the natural system (Möller  
292     and Williams-Jones, 2016) that contain low concentrations of  ${}^{\text{IV}}\text{Al}$  (up to 0.14  
293     c.f.u.) and almost no Ti or Mg.

294     The Canary Islands clinopyroxene that were selected for determination  
295     of mineral–melt partition coefficients are free from melt inclusions, suggest-  
296     ing relatively slow rates of crystal growth (Kennedy et al., 1993, Fig. 1).  
297     Chemical zonation, if present, is of a similar magnitude to the analytical  
298     precision of our electron microprobe, indicating that pressure, temperature

299 and melt composition remained stable during crystal growth. In the case of  
300 these Canary Islands clinopyroxene, the entire mineral is interpreted to be in  
301 chemical equilibrium with the adhered quenched melt. Trace-element abun-  
302 dances within these Canary Islands clinopyroxene show core-to-rim variations  
303 of about 1–5 % relative, with larger variations in element abundance asso-  
304 ciated with sector zoning than with concentric growth zoning (Supplement  
305 S1). (TO CONFIRM with images)

306 By contrast our experiment clinopyroxene display systematic composi-  
307 tional variation between their cores and rims; this variation recording changes  
308 to melt composition during growth of these crystals (e.g. Fig. 3). The sys-  
309 tematics of crystal-chemical zonation both within individual experimental  
310 charges and within groups of experiments reveal major-element exchange  
311 vectors between the clinopyroxene and the melt. Three major-element ex-  
312 change mechanisms correspond to the low ( $Ae_{5-25}$ ), medium ( $Ae_{25-50}$ ) and  
313 high ( $Ae_{55-95}$ ) aegirine domains defined above (Figs. 4b, 5 and S4).

314 **And may be used to infer.... the composition of the mineral**  
315 **assemblage that is crystallising? To discuss. Comments, please!**

316 With increasing alkali content, the Si content in clinopyroxene increases  
317 at the expense of tetrahedrally co-ordinated Al and  $Fe^{3+}$ . As aegirine content  
318 increases, substitutions at the tetrahedral site become relatively less impor-  
319 tant than exchanges at the M1 and M2 sites. At the M1 site, the substitution  
320 of Ti for ions of 2+ and 3+ valence correlates well with the exchange of tetra-  
321 hedrally coordinated 3+ cations for  $Si^{4+}$ . The exchange behaviour of 2+ and  
322 3+ cations at the M1 site depends on the aegirine content of the clinopy-  
323 roxene. In low-aegirine clinopyroxene, the concentration of 3+ ions at the

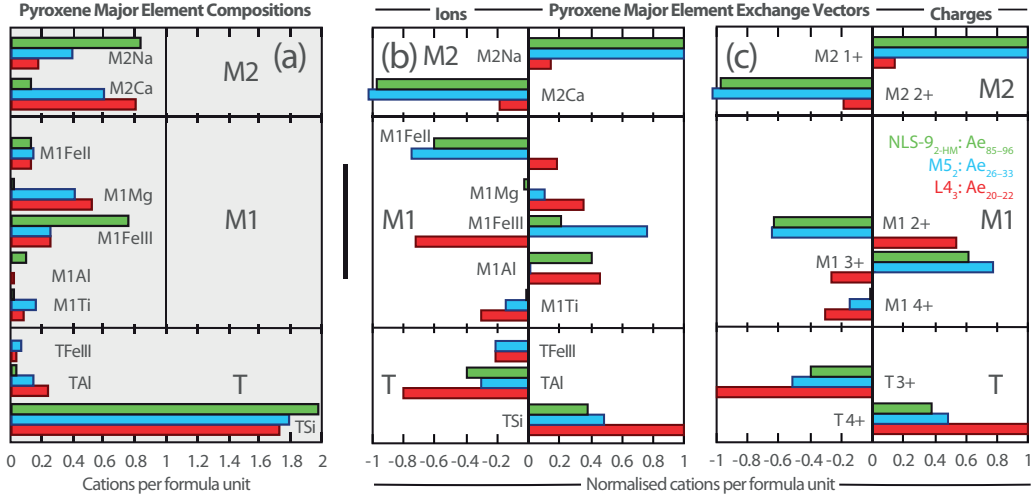


Figure 5: Bar charts showing clinopyroxene composition and major-element exchange mechanisms for three experiments representative of high (green), medium (blue) and low-aegirine (red) clinopyroxene. (a) clinopyroxene major-element compositions are expressed as cations per six-oxygen formula unit (b) exchange mechanisms grouped by ions, (c) grouped by charges. Methods used to calculate these exchange mechanisms are available in the caption of Supplementary Figure S4.

324 M1 site is negatively correlated with  $X_{Na}^{M2}$ , whereas in medium- and high-  
 325 aegirine clinopyroxene, the M1 site takes progressively more 3+ ions as  $X_{Na}^{M2}$   
 326 increases. Substitutions of Ca<sup>M2</sup> for Na<sup>M2</sup> are relatively unimportant in low-  
 327 aegirine clinopyroxene, but play a large role in medium- and high-aegirine  
 328 exchange vectors.

329 Suites of Canary Islands clinopyroxene follow similar major-element ex-  
 330 change systematics to our low aegirine experiment clinopyroxenes (CHECK,  
 331 expand if necessary).

332     4.4. Trace-element concentrations in the experiment clinopyroxene

333     Assessing the homogeneity of trace-element-concentrations within miner-  
334     als is important when defining equilibrium partition-coefficients because only  
335     the rims record true chemical equilibrium with the adjacent melt. Measure-  
336     ments of trace-element-concentrations in experimentally-grown minerals are  
337     often challenging as a result of their small size; They are commonly compara-  
338     ble in scale to the beam-size of laser-ablation or SIMS systems ( $\sim 10\text{--}20 \mu\text{m}$ ).  
339     In many cases it is therefore not possible to assess the extent to which trace-  
340     element-concentrations are zoned within experimentally-grown crystals. To  
341     assess the extent to which trace-element-concentrations are zoned within  
342     our experiment clinopyroxene, electron-microprobe transects were measured  
343     across seven crystals for the elements Mg, Fe and Ce (Supplement S3). Tran-  
344     sects were made across grains from three experiments, each crystallised to  
345     varying degrees.

346     The electron-microprobe transects reveal that clinopyroxene Ce-concentration  
347     follows both sector-zoning and concentric growth-zoning patterns, as recorded  
348     by backscattered electron images and the  $X\text{Mg}$  of the clinopyroxene. Sector-  
349     zoning has a more pronounced effect on the Ce-concentration in the clinopy-  
350     roxene than concentric growth-zoning, causing one transect to appear ‘laterally-  
351     zoned’ and another to appear ‘reverse-zoned’ in terms of Ce-concentration.  
352     These effects are due to sector-zoning, with bright sector-zones on BSE im-  
353     ages associated with higher Ce-concentrations than dark zones. To gain  
354     insight into the variation in clinopyroxene Ce-concentration associated with  
355     concentric growth-zoning, analyses were grouped *per-experiment* to average  
356     this sector-zoning effect. Ratios of median average Ce-counts / rim Ce-counts

represent the difference between the composition of the bulk crystal, as analysed by LA-ICP-MS, and the composition of the clinopyroxene rims that approach chemical equilibrium with the adjacent quenched melt and have a mean value of 1.08, ranging between 1.04 and 1.12. The highest values are found for the largest clinopyroxene crystals and in these, because of their size, we were able to avoid the cores in the analyses via LA-ICP-MS, reducing the growth-zonation bias in trace-element partition-coefficients.

Where large clinopyroxene crystals were present and time-averages of element counts could be used for the reduction of laser-ablation data, trace-element-compositions are similar among clinopyroxene crystals within individual experiments (Fig. TO ADD? Table S1) indicating that trace-element concentrations in the melt phase remained spatially homogeneous throughout the duration of the experiments. Typical trace-element concentrations in the experiment clinopyroxene are illustrated in Supplementary Figure S5c.

## 5. Discussion

### 5.1. Attainment of equilibrium in the Canary Islands rocks

The Canary Islands trace-element partition-coefficients presented here were determined from euhedral, blade-shaped crystals free of melt inclusions and chemical zonation. The corresponding quenched melt was in direct contact with these crystals and shows no zonation in backscattered electron images (Fig. 1). While equilibrium conditions are challenging to confirm for a natural volcanic system, the euhedral forms, chemical homogeneity of crystals, and congruency between samples from separate eruptions suggest that the crystals grew in a stable environment, and were not subject to chemical

<sup>381</sup> or physical perturbations during growth (Fig. 6).

<sup>382</sup> *5.2. Attainment of equilibrium in the experiments*

<sup>383</sup> Experiments used to determine trace-element partition-coefficients must  
<sup>384</sup> have attained, or at least closely approached, chemical equilibrium. Un-  
<sup>385</sup> fortunately no experiments are able to determine equilibrium trace-element  
<sup>386</sup> partition-coefficients *sensu stricto* because reversal experiments, where a  
<sup>387</sup> clinopyroxene re-equilibrates with a melt, are not possible owing to slug-  
<sup>388</sup> gish diffusion of most elements through the clinopyroxene structure (Van  
<sup>389</sup> Orman et al., 2001; Zhang et al., 2010). The following two sections discuss  
<sup>390</sup> some analytical and experimental biases that must be considered when deter-  
<sup>391</sup> mining mineral-melt trace-element partition-coefficients from crystallisation  
<sup>392</sup> experiments.

<sup>393</sup> *5.2.1. The formation of diffusive boundary layers*

<sup>394</sup> A potential barrier to chemical equilibration during crystallisation is the  
<sup>395</sup> formation of a diffusive boundary layer within the melt adjacent to growing  
<sup>396</sup> crystals. In a perfect equilibrium case there are no compositional gradients  
<sup>397</sup> in the melt at any time during crystal growth. However in reality the growth  
<sup>398</sup> of crystals depletes compatible elements from the melt and residually en-  
<sup>399</sup> riches incompatible elements. Theoretically, this process of crystal growth  
<sup>400</sup> results in formation of a (potentially ephemeral) diffusive boundary layer in  
<sup>401</sup> the melt directly adjacent to the crystal that is depleted with respect to  
<sup>402</sup> compatible elements and enriched with respect to those that are incompat-  
<sup>403</sup> ible (Lu et al., 1995). The composition of such a diffusive boundary layer  
<sup>404</sup> depends on both the relative enrichment or depletion of elements during the

405 crystallisation process, and the rate at which these elements diffuse through  
406 the melt. Rapidly-diffusing elements with partition-coefficients close to unity  
407 will have concentrations closest to that of the bulk melt.

408 Experiments designed to investigate trace-element-partitioning behaviour  
409 might employ slow cooling rates to limit the development of diffusive bound-  
410 ary layers, thus forming crystals from melt that is closer in composition to  
411 that of the bulk experiment. Such experiments then run into another prob-  
412 lem, in that significant crystallisation may occur at temperatures above that  
413 of the final run temperature. Rapidly-cooled experiments circumnavigate  
414 this issue, but may form relatively more pronounced diffusive boundary layers  
415 during crystal growth that become ‘flattened out’ during the homogenisation  
416 stage of the experiment.

417 Numerous diffusion data have been gathered for silicate melts over the  
418 past few decades, and a comprehensive review is given by Zhang et al.  
419 (2010). Diffusion of trace-elements through water-saturated peralkaline melts  
420 is rapid, owing to their depolymerised structure. For example Lanthanum  
421 diffusion-coefficients are 6 orders of magnitude higher than for water-saturated  
422 granitic compositions of a similar temperature (compare Rapp and Watson,  
423 1986; Behrens and Hahn, 2009). This rapid diffusion serves to minimise the  
424 formation of diffusive boundary layers adjacent to growing crystals in our  
425 experiments. Coupled diffusion mechanisms complicate the application of  
426 measured single-element diffusion-coefficients to a crystallising system (Grove  
427 et al., 1984; Liang et al., 1994; Costa et al., 2003). Here, the diffusive flux of  
428 trace-elements may be coupled to gradients in major-element concentration  
429 within the melt.

430 To investigate the impact of diffusive effects on trace-element-partitioning  
431 between clinopyroxene and melt, Mollo et al. (2013) performed crystallisa-  
432 tion experiments on trachybasaltic melts at a range of cooling rates (2.5–  
433 50°C / hr). Rapid cooling rates result in depletions of Si, Ca and Mg in  
434 the clinopyroxene that are compensated for by enrichments in Al, Na and  
435 Ti. Regardless of cooling rate, Ounma parabolae could be fitted through  
436 isovalent sets of partition-coefficients, indicating that crystal-lattice-effects  
437 dominated over those associated with the formation of diffusive boundary  
438 layers and that local equilibrium was achieved at the time of crystallisa-  
439 tion. In their rapidly-cooled experiments Mollo et al. (2013) found apparent  
440 clinopyroxene/melt trace-element partition-coefficients that varied with iden-  
441 tical crystal-chemical systematics to true equilibrium partition coefficients,  
442 the magnitude of both sets of trace-element partition-coefficients following  
443 the  $^{IV}\text{Al}$  content of the clinopyroxene (*ibid.*, their Fig. 9). Deviations of  
444 the partition coefficient of several orders of magnitude can be obtained only  
445 when rapidly growing crystals entrap small portions of the diffusive boundary  
446 layer that are found as minute melt inclusions randomly distributed in the  
447 mineral phase (Kennedy et al., 1993). In this extreme case, partitioning be-  
448 haviour is obviously influenced by contamination phenomena and no Onuma  
449 parabolae can be derived. As Onuma parabolae could successfully be fitted  
450 through partitioning data for all of our presented experiments (see following  
451 sections), and no melt inclusions were observed in optical and electron imag-  
452 ing, we infer that our data were not affected by the presence of such melt  
453 inclusions, and that they may be compared directly with partitioning data  
454 derived from experiments that employed slower cooling rates.

455    5.2.2. *Chemical zonation in the experiment clinopyroxene: Theoretical frame-*  
456    *work*

457    Trace-elements diffuse slowly through the clinopyroxene structure relative  
458    to that of the melt (Van Orman et al., 2001; Zhang et al., 2010), therefore no  
459    re-equilibration of trace-elements takes place on an experimental time scale.  
460    Strictly speaking, clinopyroxene only record true equilibrium conditions at  
461    their outermost rim. Experiments designed for the derivation of equilibrium  
462    partition coefficients ideally minimise bias by limiting the fraction of crystalli-  
463    sation, producing minerals that are as homogeneous as possible. Currently  
464    available *in situ* analytical techniques for trace-element abundances, such as  
465    LA-ICP-MS and SIMS, are limited in terms of minimum beam-size to  $\sim$ 10  
466     $\mu\text{m}$ ; chemical zonation, however subtle, will be continuous from the core to  
467    the rim of the mineral. Consequently, no experimentally-derived partition-  
468    coefficients record chemical equilibrium *sensu stricto*, but properly conducted  
469    experiments may closely approximate this state.

470    Because only the very rim of a crystal records chemical equilibrium with  
471    the adjacent melt, and some internal portions of the minerals must be sam-  
472    pled during *in-situ* analyses all experimentally-determined trace-element partition-  
473    coefficients are biased toward higher values for compatible elements and lower  
474    values for incompatible elements. The magnitude of these biases depends  
475    on the fraction of crystallisation in the experiment, the true equilibrium  
476    partition-coefficient of that element, as well as the proportion of each growth-  
477    zone sampled during the *in-situ* analysis. Fortunately *in-situ* chemical anal-  
478    yses preferentially sample the mantle and rim of zoned crystals because few  
479    analyses section a crystal perfectly through the core. As a result there is a

480 sampling bias toward equilibrium mineral compositions.

481 Consider a hypothetical experimental system in which 20% of the melt  
482 crystallises as a single mineral, and where the chemical analyses of that  
483 mineral are truly bulk averages of that mineral composition. An incompatible  
484 element with a true equilibrium partition coefficient of 0.1 would return a  
485 measured partition coefficient of 0.09, a small bias because the concentration  
486 of that incompatible element in the melt changed only subtly during the  
487 course of crystallisation. For compatible elements with true  $D_i$  values of  
488  $\sim 10$ , measured partition coefficients can be a factor of 2–3 higher than true  
489 partition coefficients, because their concentration in the melt changes more  
490 than an incompatible element during the course of crystallisation.

491 Further complexity is introduced in systems that crystallise multiple min-  
492 erals simultaneously. In the case of experiment M3<sub>2</sub>, the REE are compatible  
493 in clinopyroxene, but are incompatible in biotite and oxides (e.g. Mahood and  
494 Stimac, 1990; Schmidt et al., 1999). The REE have therefore been residually  
495 enriched in the melt phase by the crystallisation of biotite and oxide miner-  
496 als, while simultaneously being depleted from the melt by crystallisation of  
497 clinopyroxene. These two competing processes serve to minimise the effect of  
498 fractional crystallisation on the concentration of trace-elements in the melt  
499 and consequently derived REE partition-coefficients between clinopyroxene  
500 and melt will be closer to true equilibrium values.

501 5.2.3. *Implications of the cerium zonation across the experiment clinopyrox-  
502 ene*

503 Because of beam-size limitations and the small minerals generated in the  
504 majority of our experiments it was not possible to measure all trace-element

505 concentrations within the core and rim of experiment clinopyroxene sepa-  
506 rately. Electron-microprobe analyses offer a smaller minimum beam-size than  
507 LA-ICP-MS systems at the expense of precision and of number of elements  
508 that may be analysed simultaneously. This higher spatial resolution permit-  
509 ted investigation of the zonation of Ce concentrations within the experiment  
510 clinopyroxene, with Ce as a proxy for the other compatible elements.

511 The magnitude of concentric growth zoning in the experiment clinopy-  
512 roxene was examined by averaging bulk and rim compositions across mul-  
513 tiple sector-zoned grains within each experiment. The median Ce counts  
514 divided by the rim Ce counts was 1.04 for experiment M3<sub>2</sub>, 1.08 for ex-  
515 periment M5 and 1.12 for the fluorine-bearing experiment M3-1.25F (see  
516 Beard, 2018). Contrary to theory discussed above, the subtly (3%) crys-  
517 tallised experiment M5 shows a greater variation in core-to-rim Ce content  
518 than the more heavily (?? TO ADD%) crystallised experiment M3<sub>2</sub>. Further-  
519 more, the  $D_{Ce}^{cpx/melt}$  for experiment M3<sub>2</sub> (6.2) is approximately double that  
520 for experiment M5 (see discussion below), which should further promote the  
521 formation of Cerium zonation in the clinopyroxene during crystallisation.  
522 Consequently it is possible that many existing experimentally-derived trace-  
523 element partition-coefficients are systematically offset from true equilibrium  
524 values.

525 If Cerium is used as a proxy for the behaviour of compatible elements  
526 in our experimental system, then apparent partition coefficients derived for  
527 these elements via LA-ICP-MS are systematically offset to higher values by 4–  
528 8%. Such a systematic bias is small, relative to the variation in clinopyroxene-  
529 melt partition coefficients within our sample set, as well as in the literature.

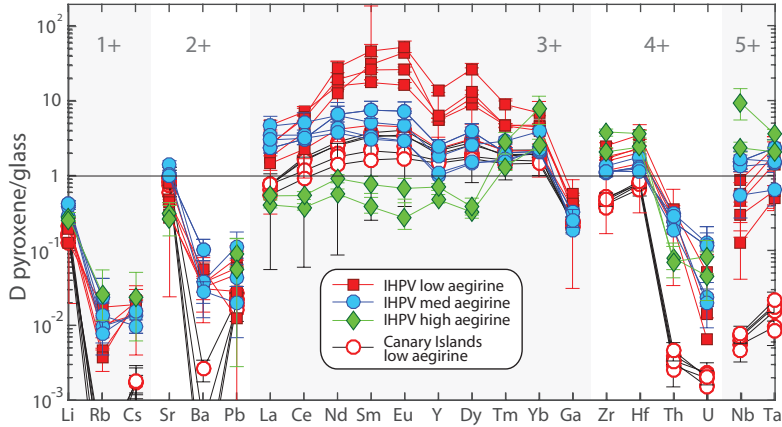


Figure 6: Trace-element partition-coefficients between clinopyroxene and silicate melt, as determined from internally heated pressure vessel experiments ( $n = 11$ ; low-, medium- and high-aegirine types) and from clinopyroxene-rim glass pairs from pyroclastic fall deposits from Tenerife, Canary Islands ( $n = 6$ ; low-aegirine type). Uncertainties on the partition coefficients are at the  $1\sigma$  level.

530 The effect of crystal zonation on incompatible element concentrations was  
 531 not measured, but as outlined in the theoretical framework above, this effect  
 532 should be smaller than that for the compatible elements. No correction factor  
 533 has been applied to the data presented in the figures below, or in Tables 4  
 534 and S1.

535 *5.3. Trace-element-partitioning*

536 Trace-element partition-coefficients and their uncertainties were calcu-  
 537 lated as mass concentration ratios between clinopyroxene and coexisting  
 538 quenched melt and are reported in Tables 4 and S1. Where trace-element-  
 539 concentrations in clinopyroxene could be determined using regular time-  
 540 averages of counts-per-second from the ICP-MS system, a time-weighted

541 average composition of clinopyroxene was used with that of the coexisting  
542 glass to calculate the trace-element partition-coefficients and their associ-  
543 ated uncertainty. Where the laser-ablation unmixing model was required for  
544 reduction of clinopyroxene trace-element analyses, the partition coefficients  
545 were calculated using time-weighted average compositions of glass alongside  
546 the corresponding ‘unmixed’ clinopyroxene trace-element concentration. Be-  
547 cause a robust-regression data reduction scheme was used, this technique re-  
548 turns a median-average trace-element concentration for clinopyroxene. This  
549 approach is preferable when compared to using a mean average because it ef-  
550 fectively rejects outlier data, for example from the ablation of minerals other  
551 than clinopyroxene that may have been hidden below the polished surfaces  
552 of the grain mounts. Uncertainty calculations are described in the caption  
553 for Figure S5.

554 Three markedly different behaviours of rare earth element partitioning are  
555 observed in the experiments (Fig. 6). These depend on the aegirine concen-  
556 tration in the clinopyroxene and match the major-element exchange vector  
557 domains discussed above. Low-aegirine experiment clinopyroxene ( $Ae_{5-25}$ )  
558 prefer the MREE; medium-aegirine clinopyroxene ( $Ae_{25-50}$ ) show a similar  
559 behaviour, save for higher LREE partition coefficients, whereas high-aegirine  
560 clinopyroxene ( $Ae_{55-95}$ ) strongly prefer HREE and show incompatible be-  
561 haviour for the light and middle REE. The experiment REE partition co-  
562 efficients are 0.3–53, typically 2–6, with minima for LREE and MREE in  
563 high-aegirine clinopyroxene (Fig. 6).

564 Our experimental REE partition coefficients are about an order of mag-  
565 nitude higher than in most other studies of clinopyroxene-melt element-

partitioning that are included in the compilation of Bédard (2014, Fig. 7d,e,f) and (Mollo et al., 2016). This compilation includes clinopyroxene–melt trace-element partition-coefficients for more than 400 samples, determined both experimentally and from natural phenocryst–melt pairs. The database covers a wide range of physicochemical conditions (0.0001–3.5 GPa, 650–1345 °C,  $\log f\text{O}_2 = \text{IW}$  to MH  $\approx \Delta\text{QFM}$  -5 to +5), clinopyroxene compositions ( $X\text{Mg}$  0.031–1,  $X_{\text{Na}}^{M2}$  0–0.84 and  $\text{Al}^T$  0–0.49 c.f.u.) and melt compositions ( $\text{Mg}\# = 0$ –100 and  $X\text{H}_2\text{O} = 0$ –0.38). In the diagrams we present separately the experimental- and natural-sample data pertaining to Italian alkaline volcanoes from the Roman Province (K-rich ‘orogenic’) and Sicily (tholeiitic to Na-alkaline ‘anorogenic’) (Wood and Trigila, 2001; Fedele et al., 2009; Mollo et al., 2013, 2016, red translucent in diagrams).

The Canary Islands clinopyroxene show similar rare-earth-element partitioning-systematics to the low-aegirine experiment clinopyroxene, with absolute values for these partition coefficients of about one order of magnitude lower, intermediate between the majority of literature data and our experiment clinopyroxene (Figs. 6, 7d–f).

The high field-strength elements (HFSE) Zr, Hf, Nb and Ta are compatible to slightly incompatible in the experimental clinopyroxene with the high-aegirine clinopyroxene displaying the highest partition coefficients for these elements. In the Canary Islands clinopyroxene, the HFSE are typically 1–2 orders of magnitude less compatible than in the experimental samples, displaying partitioning behaviour similar to literature values for these elements (Fig. 7a,b,c). Partition coefficients for the large-ion lithophile elements K, Sr, Pb are positively correlated with  $X_{\text{Na}}^{M2}$  in the low- and medium-aegirine

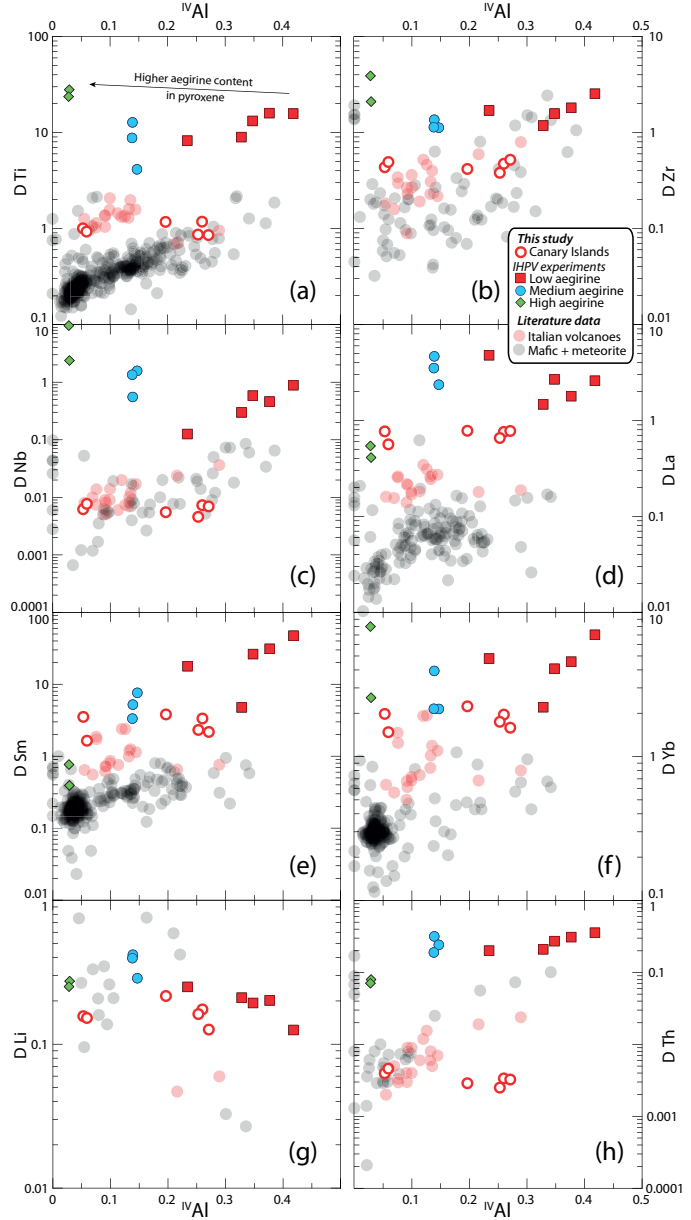


Figure 7: Element partition coefficients for HFSE (Ti, Zr, Nb), REE (La, Sm, Yb) and TE (Li, Th) vs.  $^{IV}\text{Al}$ . Literature values ( $n = 411$ ), including those from the Italian volcanoes, are from the compilation of Bédard (2014) and from Mollo et al. (2016). A similar diagram with  $X_{Na}^{M2}$  in place of  $^{IV}\text{Al}$  is in Supplement S6.

591 clinopyroxene, but are lower in high-aegirine clinopyroxene (Fig. S6). The  
592 Rb, Cs and Ba partition coefficients have a high uncertainty and are maxi-  
593 mum estimates owing to low concentrations of these elements in the clinopy-  
594 roxene, close to the detection limit for analyses by LA-ICP-MS. These data  
595 are therefore not discussed further. Lithium is incompatible ( $D_{Li} = 0.1\text{--}0.4$ )  
596 in both Canary Islands and experimental clinopyroxene and, like Sr and Pb,  
597 becomes more compatible with increasing aegirine content in the clinopy-  
598 roxene, plateauing at  $X_{Na}^{M2} = 0.4$  and decreasing thereafter (Figs. 7g, S6g).  
599 The actinides U and Th show contrasting partitioning behaviour; the former  
600 showing no correlation with aegirine content in the clinopyroxene, the latter  
601 becoming more incompatible with increasing aegirine content (Fig. 7h). The  
602 U and Th partition coefficients for our Canary Islands samples are similar  
603 to those from the Italian volcanoes and are 1–2 orders of magnitude more  
604 incompatible relative to the experimental clinopyroxene.

605 *5.4. Fits to the lattice-strain model*

606 The equilibrium partitioning of trace-elements between minerals and melts  
607 is largely controlled by the structure of the crystal lattice, its elasticity (On-  
608 uma et al., 1968; Kumazawa, 1969; Weidner and Vaughan, 1982) and its  
609 ability to accommodate an excess or shortage in charge (Blundy et al., 1998;  
610 Wood and Blundy, 2001; Hanchar et al., 2001; Corgne and Wood, 2005). The  
611 lattice-strain model provides a framework in which the influence of these vari-  
612 ables on partitioning behaviour can be quantified, and thus predicted under  
613 conditions bracketed by a calibrating data set (Onuma et al., 1968; Blundy  
614 and Wood, 1994; Wood and Blundy, 2014). Lattice structure has a depen-  
615 dence on pressure, temperature and composition, and element-partitioning

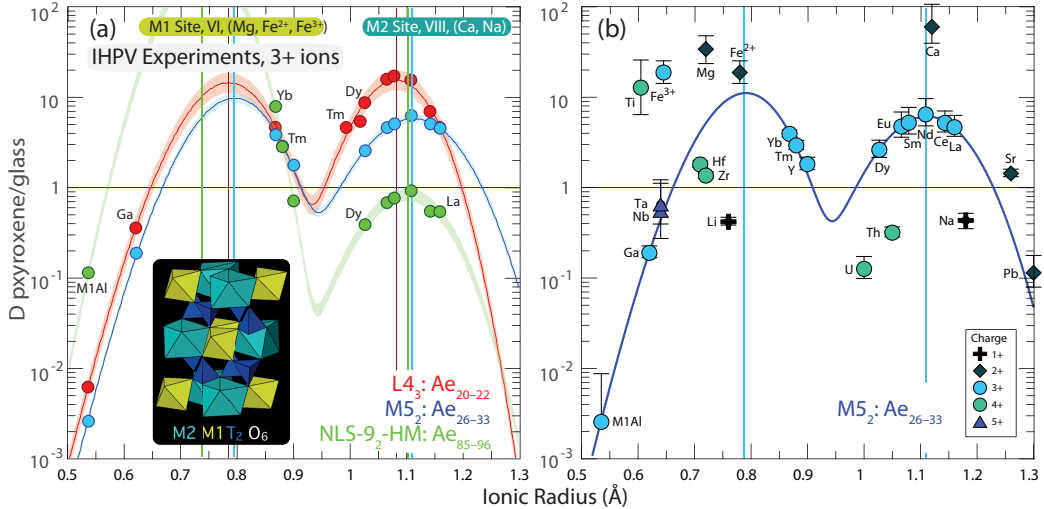


Figure 8: Non-linear weighted least-squares fits to element-partitioning data from the internally heated pressure vessel experiments following the lattice-strain model of Blundy and Wood (1994). (a) Representative fits to 3+ ion partitioning behaviour with examples for low (red), medium (blue) and high-aegirine (green) clinopyroxene experiments. (b) Measured partition coefficients for ions of 1+, 2+, 4+ and 5+ charges that are consistent with the lattice-strain model. Ionic radii are assigned to 6 or 8 fold co-ordination (Shannon, 1976), and were chosen to minimise residuals in the fit (cf. Olin and Wolff, 2010). Y was not included in the fitting routine for 3+ ions because of mass fractionation effects (ibid.). Vertical coloured lines indicate ideal ionic radii ( $r_0$ ) of M1 and M2 sites and shaded areas indicate 95% confidence intervals on the fits determined via bootstrapping. Uncertainties on the partition coefficients in (b) are  $1\sigma$ . Fitted lattice-strain parameters are given in Table 4.

is a thermodynamically-controlled process (e.g. Wood and Blundy, 1997).

Most trivalent ions, including the REE and Y enter the M2 site of clinopyroxene, which is typically 6- or 8-coordinated (Deer et al., 1992). Smaller trivalent ions, including Al, Cr, Ga, Sc, and in the case of Fe-rich clinopyrox-

ene the HREE may enter the smaller, octahedral M1 site (Olin and Wolff, 2010; Bédard, 2014). The high field-strength elements Ti, Zr, Hf, Nb and Ta are typically hosted by the M1 site (Hill et al., 2000, 2011; Dygert et al., 2014).

To investigate systematics in  $D_i$  values and the mechanisms by which trace-elements are incorporated into clinopyroxene, element-partitioning behaviour was explored in light of the lattice-strain theory, quantitatively described by the lattice-strain equation:

$$D_i^{mineral/melt} = D_0 \exp \left[ \frac{-4\pi E_s N_a}{RT} \left( \frac{r_0}{2} (r_0 - r_i)^2 - \frac{1}{3} (r_0 - r_i)^3 \right) \right] \quad (1)$$

where  $r_0$  is the ideal radius for the lattice site,  $E_s$  is the Young's modulus (i.e., the lattice site stiffness),  $D_0$  is the strain-free partition coefficient,  $N_a$  is Avagadro's number,  $R$  is the gas constant,  $T$  is temperature in Kelvin, and  $r_i$  is the ionic radius of the element in question, all radii in Å. We focused on 3+ ions that cover a wide range of radii and fitted lattice-strain parameters for both the M1 and M2 sites of clinopyroxene (Fig. 8):

$$D_i^{cpx/melt} = D_0^{M2} \exp \left[ \frac{-4\pi E_s^{M2} N_a}{RT} \left( \frac{r_0^{M2}}{2} (r_0^{M2} - r_i)^2 - \frac{1}{3} (r_0^{M2} - r_i)^3 \right) \right] + D_0^{M1} \exp \left[ \frac{-4\pi E_s^{M1} N_a}{RT} \left( \frac{r_0^{M1}}{2} (r_0^{M1} - r_i)^2 - \frac{1}{3} (r_0^{M1} - r_i)^3 \right) \right] \quad (2)$$

Parabolae for 3+ ions were fitted for the M1 and M2 sites using the REE, Ga and Al assigned to the M1 site of clinopyroxene (Fig. 8a). Fits are weighted based on uncertainties for the element-partition coefficients. HREE have higher element-partition coefficients than can predicted by substitution into

the M2 site, hence were fitted with ionic radii for sixfold coordination into the M1 site (*cf.* Olin and Wolff, 2010; Reguir et al., 2012). Lattice-strain parameters as obtained from fits to the data are shown in Table S1.

In some low-aegirine experiments and the Canary Islands rocks, lattice-strain fitting for 3+ ions at the M1 site was not possible, because too few HREE partitioned onto the M1 site of these clinopyroxene. Here, we chose to fit only lattice-strain parameters for the M2 site, or fix  $D_0^{3+}$  values for the M1 site to match those for the M2 site, and fit only the  $r_0$  and  $E_s$  parameters for the M1 site. Fitting of element-partitioning data for 1+, 2+ and 4+ ions was less successful owing to sparse coverage of suitable radii and detection-limit issues for some elements. Partition coefficients for 1+, 2+, and 4+ elements follow radius- and charge-dependent trends consistent with lattice-strain theory and reported effects of charge on lattice-strain parameters (Fig. 8b, e.g., Hazen and Finger, 1979; Law et al., 2000; Adam and Green, 2006).

#### 5.4.1. Effects of composition on ideal site size, $r_0$

As the composition of clinopyroxene shifts from augite toward aegirine, the size of the M1 and M2 sites, or strain-free radii ( $r_0$ ), should diverge following the sizes of the major-element cations on these sites. Lattice-strain fits for 3+ cations indicate expansion of the M2 site between low and medium-aegirine clinopyroxene, with  $r_{0M2}^{3+}$  correlating well with Na replacing Ca (Figs. 8, 9). Expansion of the M2 site stalls at  $r_{0M2}^{3+} \approx 1.12$  Å and  $X_{Na}^{M2} \approx 0.4$ , changing little in size between medium and high-aegirine clinopyroxene. We suggest that this is a ‘saturation effect’, whereby the smaller ions in the T and M1 sites prevent further expansion of the M2 site as additional  $R_{M2}^{+}$  is added to the clinopyroxene. For the M1 site of clinopyroxene, strain free

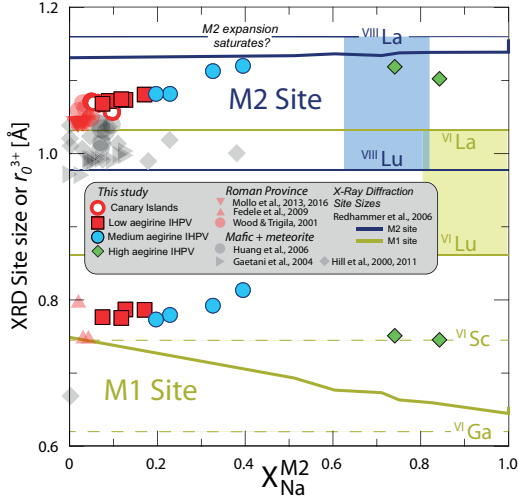


Figure 9: Diagram showing variation of ideal ionic radius  $r_0^{3+}$  with  $X_{\text{NaM2}}$  for M1 and M2 sites of clinopyroxene. Shown for comparison are single crystal x-ray diffraction data from the hedenbergite-aegirine compositional join (heavy solid lines, from Redhammer et al., 2006). Shaded boxes represent the range of ionic radii for rare earth elements in VI and VIII coordination (Shannon, 1976). Literature data for the Roman Province, Italy are from Fedele et al. (2009); Mollo et al. (2013, 2016); Wood and Trigila (2001) and for mafic systems are from Hill et al. (2000, 2011); Gaetani (2004); Huang et al. (2006).

663 radii for  $R^{3+}$  cations indicate expansion between low and medium-aegirine  
 664 clinopyroxene and contraction between medium and high-aegirine clinopy-  
 665 roxene (Figs. 8, 9). These trends broadly follow the substitution of  $\text{Mg}^{2+}$  for  
 666  $\text{Fe}^{2+}$ , then  $\text{Fe}^{2+}$  for  $\text{Fe}^{3+}$  with increasing aegirine content in the clinopyrox-  
 667 ene.

#### 668 5.4.2. The effect of cation charge on the $D_0$ parameter

669 The  $D_0$  parameter of the lattice-strain model describes ideal, strain-free  
 670 partitioning and tracks the solubility of an ideal cation in the mineral with

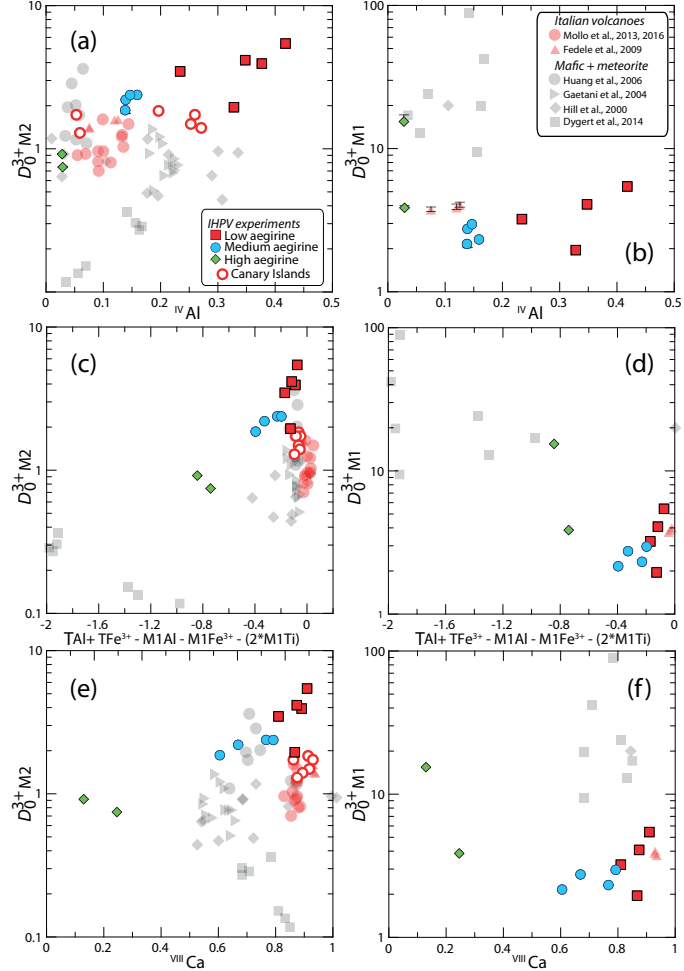


Figure 10: Strain-free partitioning coefficients ( $D_0$ ) for 3+ ions into clinopyroxene vs. various charge compensation mechanisms. (a,c,e) are for the M2 site, and (b,d,f) are for the M1 site. The diagrams show that variability in partitioning behaviour is highly dependent on mineral composition, and that variation between aegirine-rich clinopyroxene cannot be explained well by the same mechanisms as more mafic systems.  $1\sigma$  uncertainties on the  $D_0^{3+}$  values are shown in (a, b) and are usually smaller than the symbol sizes.

671 changing pressure, temperature and the bulk composition of the system  
672 (Wood and Blundy, 2014).  $D_0$  therefore correlates with the major-element  
673 composition of the clinopyroxene. Moreover, incorporation of trace-elements  
674 of a different charge introduces an electrostatic penalty that leads to a lower  
675  $D_0$  for that charge (Wood and Blundy, 2001, 2003).

676 The average charge of major-elements on the M2 site of clinopyroxene  
677 decreases from 2+ to 1+ on the compositional join between Ca-rich diopside  
678 and Na-rich aegirine. Consequently, the electrostatic penalty for substituting  
679 a REE<sup>3+</sup> cation into the clinopyroxene M2 site is increased. Indeed,  $D_{0,M2}^{3+}$   
680 decreases as Ca exchanges for Na (Fig. 10e). Conversely, as the average  
681 charge on the M1 site of clinopyroxene increases from 2+ toward 3+ in end-  
682 member aegirine, the electrostatic penalty incurred when substituting REE<sup>3+</sup>  
683 cations onto the M1 site is reduced (Fig. 10f). As a result,  $D_{0,M1}^{3+}$  increases  
684 by approximately an order of magnitude between our medium-aegirine and  
685 high-aegirine experimental clinopyroxene, an effect that when combined with  
686 the shrinking M1 site size, leads to strong fractionation of the HREE (Figs.  
687 8 and 10f).

688 A positive correlation between Al<sup>T</sup> and partition coefficients for highly  
689 charged trace-elements has been extensively documented in studies on clinopy-  
690 roxene (Lundstrom et al., 1994; Gaetani and Grove, 1995; Blundy et al., 1998;  
691 Francis and Minarik, 2008; Hill et al., 2011; Mollo et al., 2016). The low-  
692 aegirine experimental clinopyroxene and most of the Canary Islands rocks ex-  
693 tend trends defined by clinopyroxene from mafic systems (Fig. 10a), whereas  
694 the remainder of the experimental data set and Canary Islands rocks show  
695 element-partitioning behaviour similar to the potassic Roman Province of

696 Italy (Wood and Trigila, 2001; Fedele et al., 2009; Mollo et al., 2016), con-  
697 firmed that an Al<sup>T</sup>-controlled substitution mechanism extends to peralkaline  
698 conditions (Figs. 7, 10a).

699 Tetrahedral Al is thought to facilitate incorporation of REE<sup>3+</sup> cations  
700 onto the M2 site of clinopyroxene by replacing Si<sup>4+</sup>, thereby reducing local  
701 charge and thus the electrostatic penalty associated with incorporation of  
702 REE (Blundy et al., 1998). The substitution of Fe<sup>3+</sup> for tetrahedral Si<sup>4+</sup> can  
703 be expected to have a similar effect. Conversely, R<sup>3+</sup> ions on the neighbouring  
704 M1 site should hinder incorporation of REE on the M2 site, because they  
705 increase local charge by replacing R<sup>2+</sup> ions, such as Mg<sup>2+</sup> and Fe<sup>2+</sup>. This  
706 electrostatic penalty should apply doubly to Ti<sup>4+</sup> on the M1 site. This effect  
707 is consistent with our experimental data (Fig. 10c), but is not obvious in the  
708 natural samples, nor in the majority of the literature experimental data. It  
709 would thus appear that other factors, such as melt structure, have a stronger  
710 control on  $D_{REE}$  (e.g. Prowatke and Klemme, 2005).

711  $D_0^{3+}$  parameters for the M1 site are strongly correlated with those for the  
712 M2 site, except at aegirine concentrations exceeding 50 mol.%. Similarities to  
713 M2 partitioning behaviour likely reflect the dominance of T-site substitution  
714 mechanisms in augite clinopyroxene. In the high-aegirine clinopyroxene, T-  
715 site substitutions become less important as the T-sites become saturated with  
716 Si<sup>4+</sup> (Fig. 5). The replacement of Fe<sup>3+</sup> at the M1 site by 3+ trace-elements  
717 does introduce a charge penalty, therefore  $D_{0M1}^{3+}$  increases accordingly.

718 *5.5. The effects of melt structure on element-partitioning*

719 The partitioning of trace-elements between crystals and melts is con-  
720 trolled by their relative activity in each phase and the exchange mechanisms

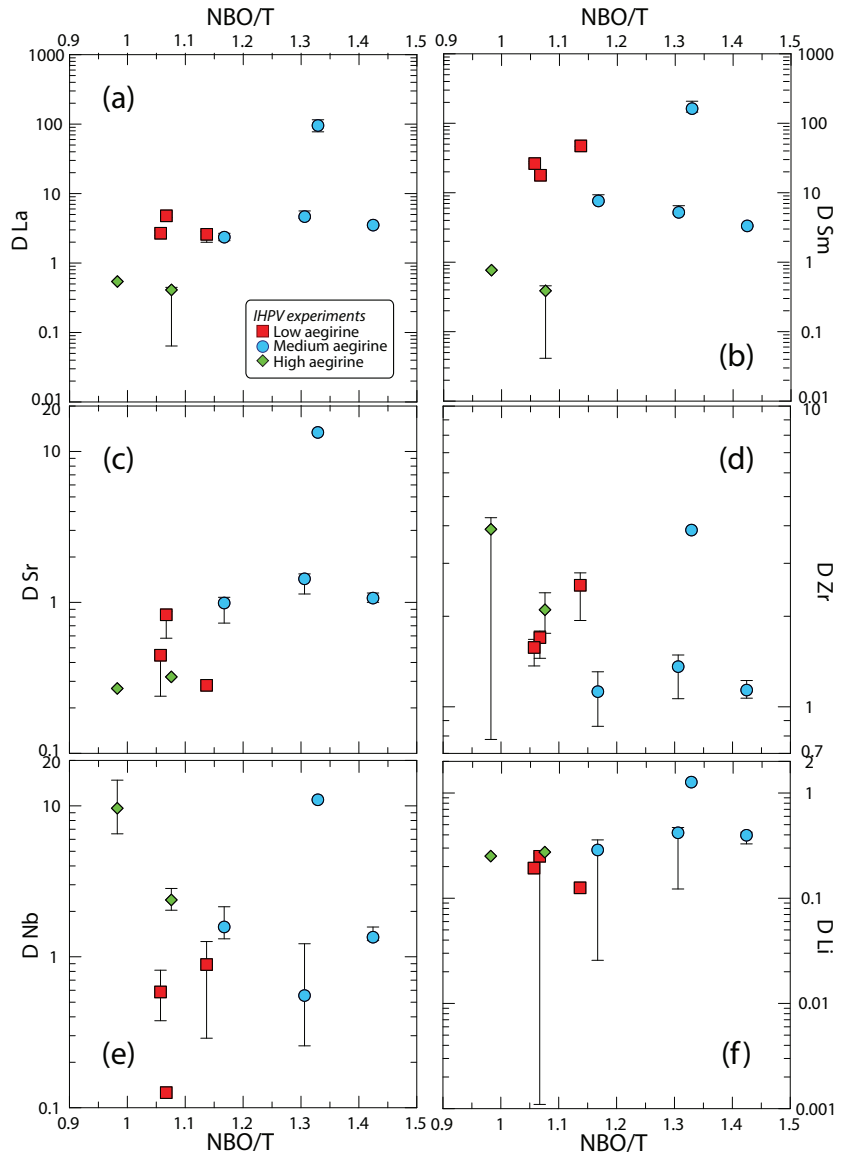


Figure 11: Diagrams of clinopyroxene–melt trace-element-partition coefficients for the IHPV experiments as a function of NBO/T of the quenched melt (Mysen et al., 1985). The water-saturated, sodic compositions investigated produce melts with highly depolymerised structures. The NBO/T ratio of these melts is not correlated with trace-element-partition coefficients, except weakly in the case of Sr. In highly polymerised systems ( $\text{NBO}/\text{T} < 0.49$ , Gaetani 2004) partition coefficients for REE and HFSE are negatively correlated with this parameter. (see Fig. 9 from Huang et al. 2006).

721 by which their incorporation into crystals takes place (e.g., Jd-melt, Jd-DiHd  
722 and CaTS-DiHd exchanges have been shown to control REE incorporation  
723 in cpx, Putirka, 2008; Wood and Blundy, 2014; Mollo et al., 2017). As such,  
724 one might expect to see correlations between melt structural parameters and  
725 trace-element-partition coefficients. Such correlations have been reported by  
726 numerous authors (e.g., Schmidt et al., 2006; Mollo et al., 2017), but appear  
727 to be expressed over a limited range of melt compositions (Gaetani, 2004;  
728 Huang et al., 2006). A widely used descriptor for melt structure is the ra-  
729 tio of non-bonding oxygen anions to tetrahedrally-coordinated cations ( $\frac{NBO}{T}$ ,  
730 Mysen et al., 1982, 1985). In relatively polymerised melts, where this ratio  
731 falls below 0.49, melt structure has been shown to have a significant influence  
732 on mineral–melt partition coefficients (Gaetani, 2004; Huang et al., 2006).

733 To calculate NBO/T for our experiments, we estimated melt Fe oxida-  
734 tion state from run temperatures and known  $fO_2$  buffer conditions (Kress  
735 and Carmichael, 1991). The recalculated total of major-element oxides (incl.  
736  $Fe_2O_3$ ) was then used to approximate the water content of the quenched  
737 melts. Oxygen from this dissolved water was added into the NBO/T cal-  
738 culation, which followed Mysen et al. (1985). The high content of alkali-  
739 lies and dissolved water in the experiments presented here produced melts  
740 that have  $NBO/T = 0.98\text{--}1.42$ ; well above the compositional boundary re-  
741 ported by Gaetani (2004). Consistent with his findings, most trace-element-  
742 partition coefficients determined from our experiments are uncorrelated with  
743 the NBO/T ratio of the melt (Fig. 11). An exception is  $D_{Sr}$  that shows  
744 a weak positive correlation with NBO/T (Fig. 11c). NBO/T could not be  
745 calculate for our Canary Islands compositions because the water content of

746 the melt prior to quench is not known.

747 Because partition coefficients between clinopyroxene and melt are con-  
748 trolled by the relative activity of elements in each of these two phases, an  
749 empirical model to predict partition coefficients from both melt and mineral  
750 compositional terms has the highest potential for accuracy. Application of  
751 such a model would however require measurement of both mineral and melt  
752 phases, which would limit its geological utility. A similar model based only  
753 on clinopyroxene composition could be applied in a wider range of scenarios  
754 where melt composition cannot be directly measured, for example to cumu-  
755 late systems or to concentrically zoned phenocrysts. Because crystallisation  
756 is a thermodynamically controlled process, the composition of the melt and  
757 thus its effects on element-partitioning will, at least in part, be recorded by  
758 the composition of the clinopyroxene. This considered, we chose to calibrate  
759 a clinopyroxene-based empirical partitioning model, based on lattice-strain  
760 theory that would be applicable over a wide compositional range from tholei-  
761 itic basalts to peralkaline phonolites. Details are provided in the following  
762 sections.

763 *5.6. An element-partitioning model extending to aegirine clinopyroxene*

764 Element partition coefficients vary systematically with the physiochemi-  
765 cal conditions of natural and synthetic magmas (cf. Wood and Blundy, 2003).  
766 Consequently, a host of models have been presented to describe the system-  
767 atics of element-partitioning between clinopyroxene and silicate melts (Wood  
768 and Blundy, 1997, 2001; Hill et al., 2011; Yao et al., 2012; Sun and Liang,  
769 2012; Bédard, 2014; Dygert et al., 2014; Mollo et al., 2016). The majority of  
770 these models are based on lattice-strain theory and predict how the lattice

771 parameters  $r_0$ ,  $E_s$ , and  $D_0$  vary with composition, temperature and pressure.  
772 This semi-thermodynamic approach theoretically permits calculation of par-  
773 tition coefficients for any trace-element, at any set of  $P - T - X$  conditions.  
774 In reality, all models have a limited working range, as restricted by the input  
775 data set. Because existing partitioning models do not reproduce the high  
776  $r_{0,M2}^{3+}$  values for clinopyroxene with aegirine contents  $\geq 50$  mol % (Fig. 12a),  
777 they cannot accurately predict REE partitioning behaviour for strongly per-  
778 alkaline systems. Here, we present a new empirical model that is calibrated  
779 on both our experimental work and natural partition coefficients from Ca-  
780 nary Islands rocks, as well as existing partitioning data from the literature  
781 (compilation of Bédard, 2014, Fig. 12, Table S1).

782 Our model focuses on the dependence of element-partitioning on clinopy-  
783 roxene composition, temperature and pressure only. While partition coeffi-  
784 cients are thermodynamically controlled by activity of elements in both the  
785 crystal and the melt phase (Wood and Blundy, 2014), and while melt struc-  
786 ture has been shown to influence element-partitioning (Huang et al., 2006;  
787 Schmidt et al., 2006; Mollo et al., 2017), it is not always possible to measure  
788 melt composition directly. For example, equilibrium melt compositions can-  
789 not be measured for the cores of zoned clinopyroxene phenocrysts in tephra,  
790 or indeed for any crystal from an intrusion in which gravitational segrega-  
791 tion of phases has occurred. Therefore, while the predictive power of a model  
792 based only on the compositions of the crystal should be lower than that of  
793 a model based on both crystal and melt compositions, a crystal-only model  
794 may be applied to a wider spectrum of geological scenarios. Melt composi-  
795 tion should, at least in part, be recorded by the major-element composition

796 of the clinopyroxene.

797 *5.6.1. The clinopyroxene M2 site*

798 To find the principal physiochemical factors that affect element-partitioning  
799 at the M2 site of clinopyroxene, a stepwise least-squares multiple linear re-  
800 gression analysis was performed using the lattice-strain parameters  $r_0^{3+}$ ,  $E_s^{3+}$   
801 and  $D_0^{3+}$ , temperature, pressure and clinopyroxene composition as inputs.  
802 Input parameters were initially examined in binary scatter diagrams to as-  
803 certain whether correlations with lattice-strain parameters were linear. If  
804 not, interaction compositional terms were added to the initial set of possible  
805 fitting parameters that had linear correlations with lattice-strain parameters  
806 (e.g.  $X_{Al+Fe^{3+}}^T$ ). Intensive variables for multiple regression models for  $r_0$ ,  
807  $E_s$  and  $D_0$  were introduced following a hierarchical forward selection crite-  
808 rion with switching. The largest number of significant terms to describe a  
809 lattice-strain parameter was eight for  $E^{M2}$  (c.95%, cf. Supplement S4).

810 Because of systematic covariation of compositional parameters in our  
811 small data set of experiments and natural samples ( $n = 16$ ), a model cal-  
812 ibrated with these points alone would be unable to deconvolve the effects  
813 of each major-element on partitioning behaviour. We have therefore added  
814 published experiments and natural phenocryst-glass pairs ( $n = 75$ ) to assem-  
815 ble a database covering a wide range of composition, pressure, temperature  
816 and oxygen fugacity (data from compilation of Bédard 2014, and Mollo et al.  
817 2016 discussed above). REE partition coefficients in this training data set  
818 vary significantly (e.g.  $D_{La}$  0.01–4.79;  $D_{Sm}$  0.02–47.24, and  $D_{Yb}$  0.11–8.00).  
819 The majority of these partition coefficients were measured via SIMS or LA-  
820 ICP-MS, minimising analytical uncertainty (e.g. from analyses by electron-

821 microprobe).

822 The resultant empirical model accounts well for changes in lattice-strain  
823 parameters over a range of compositions, faithfully reproducing large  $r_0^{M2}$   
824 values typical for sodic clinopyroxene (Fig. 12, model coefficients in Table  
825 5). Student t-tests show that all of the independent variables included in the  
826 models are significant at the 95% confidence level and PRESS  $R^2$  values were  
827 obtained by repeated by randomly subsampling the dataset (Stevens, 1996),  
828 are close to  $R^2$  values calculated by regular methods, indicating robust mod-  
829 els with high predictive power. Full multiple regression reports are available  
830 in Supplement S4. Equations generated by the multiple linear regression  
831 calculations are given below for the M2 site, where  $a_i$  are the regression co-  
832 efficients for the respective variables:

833

$$\ln D_0^{M2} = a_1 + a_2 T + a_3 X_{Al+Fe^{3+}}^T + a_4 X_{Ti}^{M1} + a_5 X_{Al-Fe^{3+}}^{M1} + a_6 X_{Fe^{2+}}^{M2} \quad (3)$$

$$E^{M2} = a_7 + a_8 P + a_9 X_{Al+Fe^{3+}}^T + a_{10} X_{Al}^{M1} + a_{11} X_{Mg}^{M1} + a_{12} X_{Ti}^{M1} \\ + a_{13} X_{Mg}^{M2} + a_{14} X_{Mg} \quad (4)$$

$$r_0^{M2} = a_{15} + a_{16} T + a_{17} X_{Al-Fe^{3+}}^{M1} + a_{18} X_{Ti}^{M1} + a_{19} X_{Ca}^{M2} + a_{20} X_{Na}^{M2} \quad (5)$$

834 The model for  $r_0^{M2}$  is robust with high predictive power and incorporates  
835 compositional controls from the M1 and M2 sites, as well as temperature.  
836 Elevated concentrations of large M2 cations  $\text{Ca}^{2+}$  and  $\text{Na}^+$  are correlated

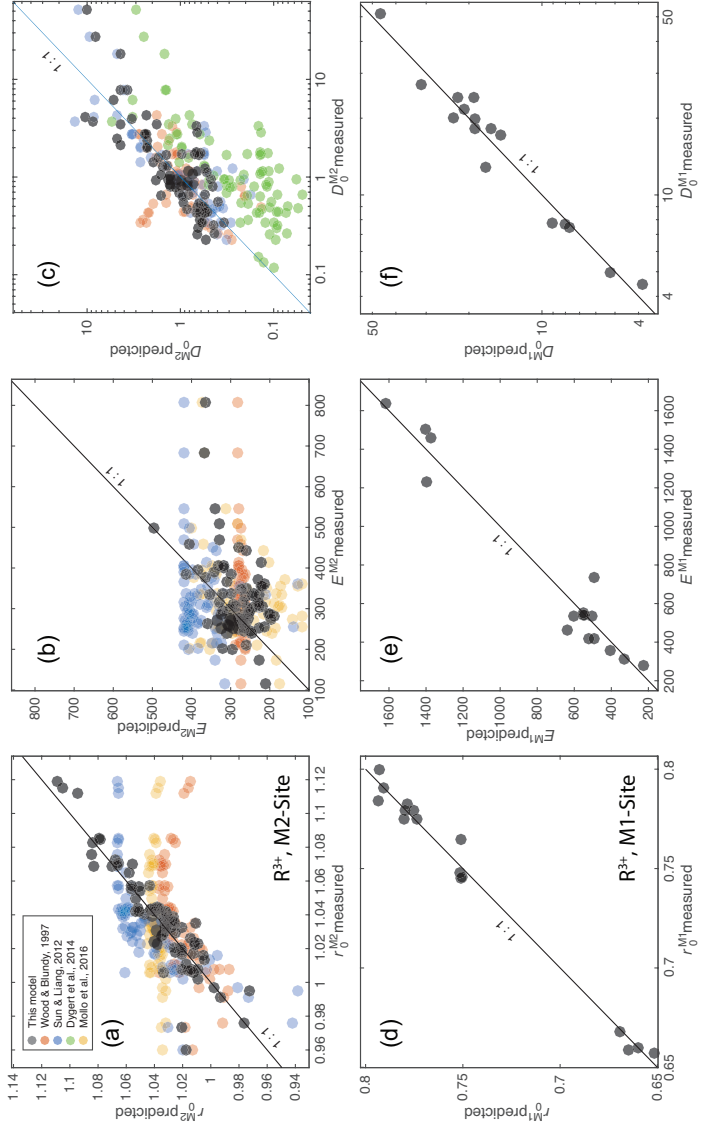


Figure 12: Measured vs. predicted model values for lattice-strain parameters for the M2 and M1 sites of clinopyroxene. The new models presented here were generated via a stepwise multiple linear regression procedure following a hierarchical forward selection criterion with switching. Full regression reports are in Supplement S4 and model equations are in the main text.

with large M2 sites.  $Ti^{4+}$  cations in the neighbouring M1 site are also correlated with expansion of the M2 site, and the concentration of small  $Al^{3+}$  minus larger  $Fe^{3+}$  on the M1 site is negatively correlated with  $r_0^{M2}$ . The negative correlation between  $r_0^{M2}$  and temperature reflects the sum of changes to major-element composition that lead to smaller clinopyroxene M2 sites at higher temperatures. This compositional effect swamps the minor influence of thermal expansion.

$D_0^{M2}$  is reasonably well predicted and incorporates compositional terms from all three sites in clinopyroxene and temperature. The positive effect of tetrahedral  $R^{3+}$  on  $D_0^{M2}$  is the largest contribution to the model, which is consistent with published studies (see above). The relationship between clinopyroxene compositional terms on the M1 and M2 sites and  $D_0$  are indirect and are tied to the solubility of the mineral in the melt (Wood and Blundy, 2003), which in turn is tied to the physiochemical conditions of the system (largely melt composition). The model for  $D_0^{M2}$  is less robust than that for  $r_0^{M2}$ , largely because there are melt compositional effects that are not recorded in the composition of the clinopyroxene. We tested the Mg# and  $XH_2O$  of the melt, neither of which are significant predictors for  $D_0^{M2}$ .

The model for  $E^{M2}$  is less well-constrained than for the other two M2 lattice-strain parameters, suggesting that M2 site stiffness is not tied strongly to clinopyroxene composition, temperature or pressure. Despite a significantly lower predictive power, this model still has physical grounding. Stiffness of the M2 site is positively correlated with pressure, as might be expected following a simple Hooke's law relationship, and there are some subtle compositional controls imparted by the T and M1 sites. The poor correlation

862 between  $E^{M2}$ , clinopyroxene composition, temperature and pressure is also  
863 evident in published element-partitioning models, where  $E^{M2}$  is either poorly  
864 predicted (Fig. 12b), or set to a fixed value (e.g. Dygert et al., 2014).

865 Diagrams of measured vs. predicted D values for R<sup>3+</sup> cations are given in  
866 Figure 13a, showing the predictive power of the models over a compositional  
867 range between basalt and peralkaline phonolite. For the M2 site, 95% of  
868 the measured R<sup>3+</sup> partition coefficients are reproduced within a factor of  
869  $\pm 2.5$  (hard dashed lines), and in extreme cases, the model still reproduces D  
870 values within an order of magnitude, sufficient for the prediction of element-  
871 partitioning trends over a wide range of  $P - T - X$ .  $D_{MREE}$ , such as Sm,  
872 are reproduced more faithfully than  $D_{LREE}$ , because their radius is closer to  
873  $r_0^{M2}$  (Fig. 13c,d), and therefore prediction of their partitioning behaviour is  
874 affected less strongly by inaccuracies in predicted  $E^{M2}$  values.

875 *5.6.2. The clinopyroxene M1 site*

876 Using a methodology similar to the M2 site, we fitted a predictive model  
877 for partitioning of R<sup>3+</sup> cations onto the smaller, 6-coordinated M1 site of  
878 clinopyroxene. Lattice-strain parabola were constrained by partitioning data  
879 for Cr, Ga, Sc, and where suitable, the HREE Tm, Yb and Lu (Our IHPV  
880 experiments plus Hill et al. 2000; Fedele et al. 2009; Mollo et al. 2013; Dygert  
881 et al. 2014). The training data set for the M1 site partitioning model is  
882 small relative to that for the M2 site ( $n = 18$ ), and because it is strongly  
883 skewed toward alkaline compositions, it has lower predictive power and is  
884 not recommended for application to mafic magmatic systems. Equations for  
885 the M1 site lattice-strain parameters, as generated by multiple linear least  
886 squares regression, are given below and shown in Figure 12 where  $b_i$  are the

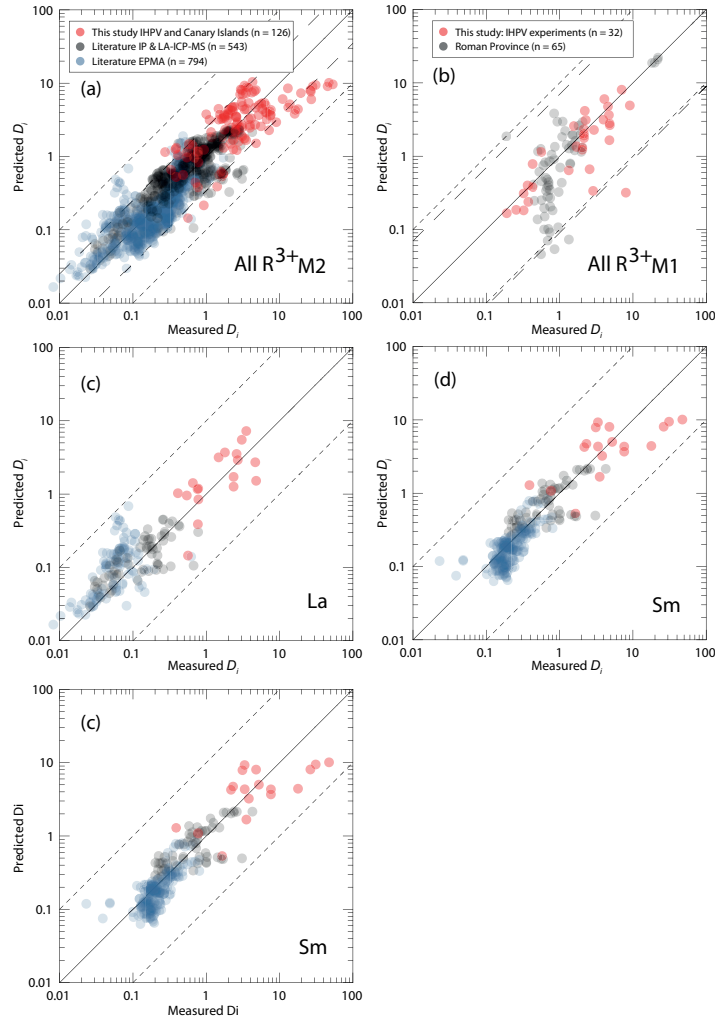


Figure 13: Measured clinopyroxene–silicate melt partition coefficients for 3+ cations vs. those predicted by our empirical model. (a) shows a comparison between measured partition coefficients and model-derived values for the M2 site of clinopyroxene. Hard dashed lines represent 95% confidence intervals of the model, and correspond to maximum uncertainties of factor  $\frac{+2.5}{-2.9}$ . Fine dashed lines represent 1 order of magnitude uncertainty (extreme outliers for M2 model). Partition coefficients in this diagram are the REE La to Er for our IHPV experiments, Canary Islands rocks, and literature data from the Italian volcanoes (Wood and Trigila, 2001; Fedele et al., 2009; Mollo et al., 2013, 2016), and all the REE plus Y for the rest of the data compilation (Bédard, 2014), which is split by analytical methodology. (b) shows performance of the predictive model for the M1 site that is calibrated for alkaline magmatic systems, and includes data from our IHPV experiments and from the Italian volcanoes. Maximum uncertainties at the 95% confidence interval are a factor of  $\frac{+7}{-11}$ , higher than for the M2 site because of the smaller calibrating data set. (c) performance of the M2 site model for La, and (d) for Sm.

887 regression coefficients (Table 5) for the respective variables:

$$\ln D_0^{M1} = b_1 + b_2 X_{Al}^T + b_3 X_{Fe^{2+}}^{M1} + b_4 X_{Ca}^{M2} + b_5 X_{Na}^{M2} \quad (6)$$

$$E^{M1} = b_6 + b_7 T + b_8 P + b_9 X_{Mg}^{M1} \quad (7)$$

$$r_0^{M1} = b_{10} + b_{11} P + b_{12} X_{Mg}^{M2} + b_{13} X_{Fe^{3+}}^{M1} + b_{14} X_{Ca}^{M2} \quad (8)$$

888 The model for  $r_0^{M1}$  is robust and accurately reproduces the input data  
889 set. A negative pressure term may reflect compressional strain on the crystal  
890 lattice. Large Fe<sup>3+</sup> cations have a positive effect on the size of the M1 site,  
891 while smaller Mg<sup>2+</sup> cations on the neighbouring M2 site have a negative effect  
892 on M1 site size. The small negative  $X_{Ca}^{M2}$  term is indirectly related to the  
893 size of the M1 site.

894  $E^{M1}$  is predicted more accurately than  $E^{M2}$  and is largely described by  
895 variations in temperature and pressure. Much like the M2 site, stiffness of  
896 the M1 site appears to be controlled dominantly by physicochemical factors  
897 that are not recorded in the composition of the clinopyroxene.

898 The model for  $D_0^{M1}$  contains compositional terms from all three crystal-  
899 lographic sites in clinopyroxene.  $X_{Al}^T$  has a strong positive correlation with  
900  $D_0^{M1}$ , consistent with a charge compensation mechanism that aids incorpora-  
901 tion of R<sup>3+</sup> cations, while terms for M1 and M2 site cations may be indirectly  
902 recording melt compositional effects. Because  $D_0^{M1}$  is unusually high for our

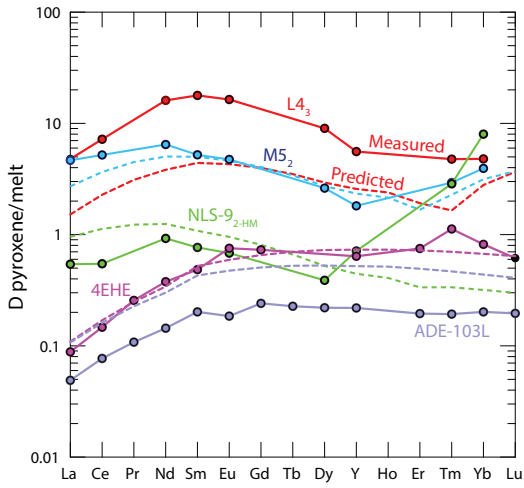


Figure 14: Measured and predicted element-partition coefficients for  $\text{REE}^{3+}$ . The model does not introduce notable radius-dependent biases, except for in our high-aegirine clinopyroxene (NLS-9<sub>2</sub>-HM in green) for which  $D_{\text{HREE}}$  are strongly underpredicted, owing to inaccurate return of  $D_0^{M1}$ . Shown for comparison are two diopside–melt pairs: 4EHE from Hill et al. (2000), grown from a synthetic (NCMAS) basaltic andesite composition and ADE-103L from Lofgren et al. (2006) grown from a picritic composition based on the Angra dos Reis meteorite.

903 high-aegirine experiments, they had to be excluded from the fitting procedure  
904 to permit model convergence. The models for  $r_0^{M1}$  and  $E^{M1}$  are calibrated  
905 for use all the way to end-member aegirine, but this was not possible for the  
906  $D_0^{M1}$  term, which is calibrated for use up to  $\sim\text{Ae}_{50}$ . Further experiments  
907 at conditions between those that generated our medium and high-aegirine  
908 clinopyroxene would be required to better constrain the clinopyroxene com-  
909 positional record of  $D_0^{M1}$  in strongly peralkaline Fe-rich magmas.

910 When applied to our experimental data, and the compilation of partition  
911 coefficients from the Roman Province (Fedele et al., 2009; Mollo et al., 2013,  
912 2016), the M1 stepwise model reproduces element-partitioning data to a fac-  
913 tor of  $\frac{+7}{-11}$  at the 95% confidence interval (Fig. 13b). Full regression reports  
914 are provided in Supplement S4.

915 For convenience, we provide an EXCEL spreadsheet for calculation of  
916 clinopyroxene-melt element-partition coefficients for any trace-element of 3+  
917 valence that is large enough to fit onto the M1 or M2 sites of clinopyroxene  
918 (Supplement S5). To assess the utility of the partitioning models and to  
919 monitor for potential introduction of radius-dependent bias, we show pre-  
920 dicted REE patterns normalised to measured ratios for some literature data  
921 and our internally heated pressure vessel experiments (Fig. 14). The model  
922 accurately reproduces REE patterns at all compositions, except for HREE  
923 on the M1 site of clinopyroxene at aegirine contents exceeding  $\sim 50$  mol%  
924 (NLS experiments).

925 *5.7. Implications for formation of REE deposits in evolved alkaline intrusions*

926 The solubility of REE and HFSE minerals is strongly enhanced in peral-  
927 kaline melts (Watson, 1979; Linnen and Keppler, 1997; Boehnke et al., 2013;

928 Aseri et al., 2015), thus the high concentration of these elements in peralka-  
929 line systems may (partially) reflect this fact (Dostal, 2017). Melts containing  
930 high concentrations of REE and HFSE are thought to be generated through  
931 low degrees of partial melting in the source, followed by residual enrichment  
932 during protracted fractional crystallisation (Marks and Markl, 2017). The  
933 budget of REE and HFSE in a fractionating magma is influenced by the  
934 mineralogy of the crystallising assemblage, and the extent to which these  
935 elements are incorporated at minor or trace concentrations.

936 Pyroxene is a major ferromagnesian phase that is commonly saturated  
937 throughout the entire differentiation histories of peralkaline magmatic sys-  
938 tems (Ablay et al., 1998; Marks and Markl, 2001; Möller and Williams-Jones,  
939 2016). The composition of the fractionating clinopyroxene has a major im-  
940 pact on the absolute REE concentrations and REE pattern of the resid-  
941 ual melt, and ultimately on the ability of a system to develop economic  
942 concentrations of the REE (Fig. 15, e.g. Kogarko, 1990; Sørensen, 1992;  
943 Marks et al., 2011). Pyroxene in alkaline magmatic systems is initially cal-  
944 cic for mafic melts, and becomes increasingly sodic as crystal fractionation  
945 proceeds (Marks et al., 2004). Although the REE are compatible in the  
946 majority of our experimentally generated clinopyroxene, those approaching  
947 aegirine end-member composition, as found in evolved alkaline magmatic  
948 systems have the lowest  $D_{REE}$  values (Fig. 6). Strongly alkaline magmatic  
949 systems are thought to crystallise abundant Ca-pyroxene early in their evolu-  
950 tion which may deplete residual liquids with respect to REEs. Consequently,  
951 even though crystallisation of Na-pyroxene could enrich residual liquids with  
952 REE, the resultant concentration of these metals in the melt would remain

953 low. However, clinopyroxene is not the only phase to crystallise from alkaline  
954 magmas, and the majority of additional silicate phases, such as olivine, bi-  
955 otite and feldspar have  $D_{REE} << 1$ , typically 1-4 orders of magnitude lower  
956 than clinopyroxene (Larsen, 1979; Kovalenko et al., 1988; Mahood and Sti-  
957 mac, 1990; Fedele et al., 2015). Consequently, if the mode of clinopyroxene  
958 is low enough, the bulk  $D_{REE}$  of the crystallising assemblage would remain  
959 below unity, allowing the REE to become enriched in the residual silicate  
960 melt.

961 To give insight into the optimum conditions for residual magmatic en-  
962 richment of the REE in alkaline systems we modelled the evolution of REE  
963 concentrations in the melt during fractional crystallisation of a nepheline  
964 syenite body (Fig. 15). Phase relation data and clinopyroxene compositions  
965 are from the experimental study of Giehl et al. (2013). Their starting com-  
966 position, based on the MiKa dyke, from the Gardar Province, Greenland, is  
967 already extremely evolved, with  $Mg\# = 2$ ,  $(Na + K)/Al = 1.44$  and  $FeO^*$   
968  $= 12$  wt.%.

969 In these models, crystallisation under water-bearing, oxidising conditions  
970 produces a high fraction of clinopyroxene that depletes residual melts with  
971 respect to Sm, while subtly enriching La. Dry conditions promote abun-  
972 dant alkali feldspar (Afs) crystallisation, which effectively enriches the REE  
973 content of residual melts. Under oxidising, dry conditions, the La/Sm ra-  
974 tio of the residual melt increases with fractionation, because Sm is more  
975 effectively incorporated into clinopyroxene. Residual enrichment is most ef-  
976 fective under dry, reducing conditions because of a relatively lower fraction  
977 of clinopyroxene within the crystallising assemblage. Because of this, the

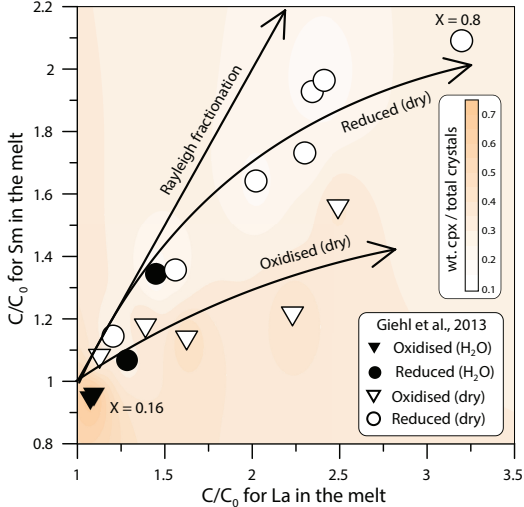


Figure 15: Model enrichment paths for La and Sm in residual melts during fractional crystallisation of a MiKa dyke composition (Gardar Province, Greenland, see Marks and Markl 2003). Phase relations and clinopyroxene compositions are from Giehl et al. (2013) and pertain to both oxidising and reducing conditions ( $\log f\text{O}_2 = \Delta\text{QFM} -3$  and +1), nominally dry to water bearing (to 3 wt.%  $\text{H}_2\text{O}$  at 1 kbar). Colour shading indicates the weight fraction of clinopyroxene within the crystallising assemblage. Bold arrows indicate residual enrichment pathways for the REE in the melt for Rayleigh fractionation (no incorporation into crystals), reduced, dry conditions, and oxidised dry conditions (the latter two are hand drawn fits to the data). For simplicity, this model does not consider REE incorporation into magnetite, alkali-feldspar, olivine, nepheline or aenigmatite, all phases generated in the experiments of Giehl et al. (2013) (see Larsen, 1979; Kovalenko et al., 1988; Mahood and Stimac, 1990).

978 REE enrichment path of the residual melt is close to that of ideal Rayleigh  
 979 fractionation. Under these reducing, dry conditions and at a temperature of  
 980 750°C, the experiments of Giehl et al. (2013) attained a crystal fraction of  
 981 0.8. Here, residual melts would have and 3.2 times La concentration and 2

982 times the Sm concentration relative to their starting composition.

983 Considering these mechanisms, alongside our experimental and Canary  
984 Islands data, the best systems to develop high REE concentrations are those  
985 that would produce small proportions of Ca-pyroxene early in their crystalli-  
986 sation histories, quickly evolving to more sodic compositions that crystallise  
987 aegirine clinopyroxene. Cooling under low-pressure, dry, reducing conditions  
988 produces abundant alkali feldspar that in the case of a peralkaline compo-  
989 sition, would serve to further increase the alkalinity of the residual melt.  
990 Low degrees of source melting would produce primary melts with (1) high  
991 REE concentrations and (2) low melt Mg + Fe, and low modal abundance  
992 of clinopyroxene, which would aid enrichment in residual melts via fractional  
993 crystallisation.

994 The HREE-rich nature of peralkaline magmatic systems, both granites  
995 and nepheline syenites, is compatible with fractionation of moderately sodic  
996 clinopyroxene that have high  $D_{LREE}/D_{HREE}$  (e.g. Möller and Williams-  
997 Jones, 2016; Dostal, 2017). As crystal fractionation progresses and clinopy-  
998 roxene compositions evolve toward the aegirine end-member composition,  
999  $D_{LREE}/D_{HREE}$  decreases (Fig. 6). This systematic change in element-  
1000 partitioning behaviour would result in strong HREE enrichment in aegirine-  
1001 pyroxene cumulates, and would enrich the residual melt with respect to  
1002 LREE-MREE.

## 1003 Conclusions

- 1004 • Our experiments reveal three distinct element-partitioning behaviours  
1005 for Na-rich clinopyroxene that depend on aegirine content. Each of

1006 these is associated with a distinct major-element exchange vector. We  
1007 do not have the compositional resolution to know if the transition be-  
1008 tween these behaviours is smooth or step-like.

- 1009 • Fits to the lattice-strain model of Blundy and Wood (1994) indicate  
1010 expansion of the M2 site with increasing  $\text{Na}_{\text{M}2}^{+}$ , to a maximum  $r_{0,\text{M}2}^{3+}$  of  
1011 1.12 Å at  $\text{Na}_{\text{M}2}^{+} = 0.4$  c.f.u. Further expansion did not occur at higher  
1012 Na contents.
- 1013 • Both the M1 and M2 sites shrink at high-aegirine contents in response  
1014 to increasing  $\sum \text{R}_{\text{M}1}^{3+}$ .
- 1015 • Charge effects lead to a progressive increase in  $D_0^{\text{M}1}$  at the expense  
1016 of  $D_0^{\text{M}2}$ , as the exchanges  $\text{Ca}^{2+}$  for  $\text{Na}^{+}$  and  $\text{M}^{2+}$  for  $\text{Fe}^{3+}$  take place.  
1017 Much like in systems of lower alkalinity, REE incorporation into clinopy-  
1018 roxene is dominated by coupled Al–Si substitutions at the T-site.
- 1019 • Existing predictive models for clinopyroxene/melt element-partitioning  
1020 do not accurately reproduce the large M2 site ( $r_{0,\text{M}2}^{3+}$ ) of clinopyroxene  
1021 with aegirine content exceeding 50 mol%. We have calibrated a new  
1022 empirical model that may be applied to any composition between basalt  
1023 and peralkaline phonolite, based on our data from experiments and  
1024 natural systems, as well as a large compilation of partition coefficients  
1025 from the literature.
- 1026 • Element partitioning systematics suggest that nepheline syenites which  
1027 host REE deposits must originate from low-degree melts with sufficient  
1028 alkali enrichment to saturate clinopyroxene similar to our medium-

1029 aegirine minerals ( $\text{Ae}_{25--50}$ ). Fractionation of such clinopyroxene en-  
1030 riches residual melts with respect to the HREE, in accord with the  
1031 composition of REE-mineralised nepheline syenite systems.

1032 **Acknowledgements**

1033 We thank the Geo.X partners GFZ and Universität Potsdam for access to  
1034 the HP-GeoMatS Lab, Don Baker for assistance with preparation of starting  
1035 materials, Bruce Watson and Volker Möller for providing samples of Mud  
1036 Tank zircon and the Nechalacho rocks, respectively, Hans Peter Nabein,  
1037 Maria Stuff and Julia Pohlenz for assistance with HP experimental equip-  
1038 ment, Toby Soutar for help with preparation of the Canary Islands samples,  
1039 Lang Shi and Glenn Poirier for assistance with electron-microprobe analyses,  
1040 and Anna Jung for assistance with laser ICP-MS analyses. The manuscript  
1041 benefited from discussions with Longbo Yang, Rebecca Paisley, Shane Rooy-  
1042 akkers and Jean Bédard. Silvio Mollo, Lorenzo Fedele and an anonymous  
1043 reviewer are thanked for their insightful feedback. Nelson Eby is thanked for  
1044 editorial handling. This work was funded by PhD scholarships to C.B. from  
1045 Geotop, DIVEX, and the SEG Canada Foundation, and operating grants to  
1046 V.vH. and J.S. from the Natural Sciences and Engineering Research Coun-  
1047 cil of Canada (grant numbers RGPIN-2014-05955, RGPAS-462335-2014) and  
1048 the FQRNT team research project program.

1049 **References**

1050 Ablay, G.J., Carroll, M.R., Palmer, M.R., Martí, J., Sparks, R.S.J.,  
1051 1998. Basanite–phonolite lineages of the Teide–Pico Viejo volcanic

- 1052 complex, Tenerife, Canary Islands. *Journal of Petrology* 39, 905–936.  
1053 doi:10.1093/petroj/39.5.905.
- 1054 Ablay, G.J., Ernst, G.G.J., Marti, J., Sparks, R.S.J., 1995. The 2 ka sub-  
1055 plinian eruption of Montaña Blanca, Tenerife. *Bulletin of Volcanology* 57,  
1056 337–355. doi:10.1007/BF00301292.
- 1057 Adam, J., Green, T., 2006. Trace element partitioning between mica- and  
1058 amphibole-bearing garnet lherzolite and hydrous basanitic melt: 1. Exper-  
1059 imental results and the investigation of controls on partitioning behaviour.  
1060 *Contributions to Mineralogy and Petrology* 152, 1–17. doi:10.1007/s00410-  
1061 006-0085-4.
- 1062 Akasaka, M., Onuma, K., 1980. The join CaMgSi<sub>2</sub>O<sub>6</sub>-CaFeAlSiO<sub>6</sub>-  
1063 CaTiAl<sub>2</sub>O<sub>6</sub> and its bearing on the Ti-rich fassaitic pyroxenes. *Contribu-*  
1064 *tions to Mineralogy and Petrology* 71, 301–312. doi:10.1007/BF00371672.
- 1065 Albert, H., Costa, F., Martí, J., 2015. Timing of magmatic processes and  
1066 unrest associated with mafic historical monogenetic eruptions in Tenerife  
1067 Island. *Journal of Petrology* 56, 1945–1966. doi:10.1093/petrology/egv058.
- 1068 Andújar, J., Scaillet, B., 2012. Experimental constraints on parameters con-  
1069 trolling the difference in the eruptive dynamics of phonolitic magmas: the  
1070 case of Tenerife (Canary Islands). *Journal of Petrology* 53, 1777–1806.  
1071 doi:10.1093/petrology/egs033.
- 1072 Aseri, A.A., Linnen, R.L., Che, X.D., Thibault, Y., Holtz, F., 2015. Effects of  
1073 fluorine on the solubilities of Nb, Ta, Zr and Hf minerals in highly fluxed

- 1074 water-saturated haplogranitic melts. *Ore Geology Reviews* 64, 736–746.
- 1075 doi:10.1016/j.oregeorev.2014.02.014.
- 1076 Beard, C.D., 2018. Mineral-melt trace element partitioning in alkaline mag-
- 1077 matic systems. Phd thesis. McGill University, Montreal, Canada.
- 1078 Bédard, J.H., 2014. Parameterizations of calcic clinopyroxene - Melt trace
- 1079 element partition coefficients. *Geochemistry, Geophysics, Geosystems* 15,
- 1080 303–336. doi:10.1002/2013GC005112.
- 1081 Behrens, H., Hahn, M., 2009. Trace element diffusion and viscous flow in
- 1082 potassium-rich trachytic and phonolitic melts. *Chemical Geology* 259, 63–
- 1083 77. doi:10.1016/j.chemgeo.2008.10.014.
- 1084 Berndt, J., Liebske, C., Holtz, F., Freise, M., Nowak, M., Ziegenbein,
- 1085 D., Hurkuck, W., Koepke, J., 2002. A combined rapid-quench and H<sub>2</sub>-
- 1086 membrane setup for internally heated pressure vessels: description and
- 1087 application for water solubility in basaltic melts. *American Mineralogist*
- 1088 87, 1717–1726. doi:10.1029/JB089iB10p08540.
- 1089 Blundy, J., Wood, B., 1994. Prediction of crystal–melt partition coefficients
- 1090 from elastic moduli. *Nature* 372, 452–454. doi:10.1038/372452a0.
- 1091 Blundy, J.D., Robinson, J.A.C., Wood, B.J., 1998. Heavy REE are compat-
- 1092 ible in clinopyroxene on the spinel lherzolite solidus. *Earth and Planetary*
- 1093 *Science Letters* 160, 493–504. doi:10.1016/S0012-821X(98)00106-X.
- 1094 Boehnke, P., Watson, E.B., Trail, D., Harrison, T.M., Schmitt, A.K.,
- 1095 2013. Zircon saturation re-revisited. *Chemical Geology* 351, 324–334.
- 1096 doi:10.1016/j.chemgeo.2013.05.028.

- 1097 Borchert, M., Wilke, M., Schmidt, C., Cauzid, J., Tucoulou, R., 2010. Partitioning of Ba, La, Yb and Y between haplogranitic melts and aqueous solutions: An experimental study. *Chemical Geology* 276, 225–240.  
1098  
1099  
1100 doi:10.1016/j.chemgeo.2010.06.009.
- 1101 Boudreau, A.E., 2004. PALLADIUM, a program to model the chromatographic separation of the platinum-group elements, base metals and sulfur in a solidifying pile of igneous crystals. *Canadian Mineralogist* 42, 393–403.  
1102  
1103  
1104 doi:10.2113/gscanmin.42.2.393.
- 1105 Brown, R.J., Barry, T.L., Branney, M.J., Pringle, M.S., Bryan, S.E., 2003. The Quaternary pyroclastic succession of southeast Tenerife, Canary Islands: explosive eruptions, related caldera subsidence, and sector collapse. *Geological Magazine* 140, 265–288. doi:10.1017/S0016756802007252.  
1106  
1107  
1108
- 1109 Bryan, S.E., Martí, J., Cas, R.A.F., 1998. Stratigraphy of the Bandas del Sur Formation: an extracaldera record of Quaternary phonolitic explosive eruptions from the Las Cañadas edifice, Tenerife (Canary Islands). *Geological Magazine* 135, 605–636. doi:null.  
1110  
1111  
1112
- 1113 Carracedo, J.C., Badiola, E.R., Guillou, H., Paterne, M., Scaillet, S., Torrado, F.J.P., Paris, R., Fra-Paleo, U., Hansen, A., 2007. Eruptive and structural history of Teide Volcano and rift zones of Tenerife, Canary Islands. *Geological Society of America Bulletin* 119, 1027–1051.  
1114  
1115  
1116  
1117 doi:10.1130/B26087.1.
- 1118 Carroll, M.R., Blank, J.G., 1997. The solubility of H<sub>2</sub>O in phonolitic melts. *American Mineralogist* 82, 549–556. doi:10.1093/petrology/32.5.1021.  
1119

- 1120 Chou, I.M., 1986. Permeability of precious metals to hydrogen at 2 kb total  
1121 pressure and elevated temperatures. *American Journal of Science* 286,  
1122 638–658.
- 1123 Corgne, A., Wood, B.J., 2005. Trace element partitioning and substitu-  
1124 tion mechanisms in calcium perovskites. *Contributions to Mineralogy and*  
1125 *Petrology* 149, 85–97. doi:10.1007/s00410-004-0638-3.
- 1126 Costa, F., Chakraborty, S., Dohmen, R., 2003. Diffusion coupling between  
1127 major and trace elements and a model for the calculation of magma cham-  
1128 ber residence times using plagioclase. *Geochimica et Cosmochimica Acta*  
1129 67, 2189–2200. doi:10.1016/S0016-7037(00)01345-5.
- 1130 Coumans, J.P., Stix, J., Clague, D.A., Minarik, W.G., Layne, G.D., 2016.  
1131 Melt-rock interaction near the Moho: Evidence from crystal cargo in lavas  
1132 from near-ridge seamounts. *Geochimica et Cosmochimica Acta* 191, 139–  
1133 164. doi:10.1016/j.gca.2016.07.017.
- 1134 Deer, W.A., Howie, R.A., Zussman, J., 1992. An introduction to the rock-  
1135 forming minerals. Longman Group Ltd, New York.
- 1136 Dostal, J., 2017. Rare earth element deposits of alkaline igneous rocks. *Re-*  
1137 *sources* 6, 1–12. doi:10.3390/resources6030034.
- 1138 Downes, H., Balaganskaya, E., Beard, A., Liferovich, R., Demaiffe, D.,  
1139 2005. Petrogenetic processes in the ultramafic, alkaline and carbonatitic  
1140 magmatism in the Kola Alkaline Province: A review. *Lithos* 85, 48–75.  
1141 doi:10.1016/j.lithos.2005.03.020.

- 1142 Droop, G.T.R., 1987. A general equation for estimating Fe<sup>3+</sup> concentrations  
1143 in ferromagnesian silicates and oxides from microprobe analyses, using  
1144 stoichiometric criteria. *Mineralogical magazine* 51, 431–435.
- 1145 Dygert, N., Liang, Y., Sun, C., Hess, P., 2014. An experimental study of  
1146 trace element partitioning between augite and Fe-rich basalts. *Geochimica  
1147 et Cosmochimica Acta* 132, 170–186. doi:10.1016/j.gca.2014.01.042.
- 1148 Edgar, C.J., Wolff, J.A., Olin, P.H., Nichols, H.J., Pittari, A., Cas, R.A.F.,  
1149 Reiners, P.W., Spell, T.L., Martí, J., 2007. The late Quaternary Diego Hernan-  
1150 nandez Formation, Tenerife: Volcanology of a complex cycle of voluminous  
1151 explosive phonolitic eruptions. *Journal of Volcanology and Geothermal Re-  
1152 search* 160, 59–85. doi:10.1016/j.jvolgeores.2006.06.001.
- 1153 Eugster, H.P., Wones, D.R., 1962. Stability relations of the ferruginous bi-  
1154 otite, annite. *Journal of Petrology* 3, 82–125. doi:10.1093/petrology/3.1.82.
- 1155 Fedele, L., Lustrino, M., Melluso, L., Morra, V., Zanetti, A., Van-  
1156 nucci, R., 2015. Trace-element partitioning between plagioclase, alkali  
1157 feldspar, Ti-magnetite, biotite, apatite, and evolved potassic liquids from  
1158 Campi Flegrei (Southern Italy). *American Mineralogist* 100, 233–249.  
1159 doi:10.2138/am-2015-4995.
- 1160 Fedele, L., Zanetti, A., Morra, V., Lustrino, M., Melluso, L., Vannucci,  
1161 R., 2009. Clinopyroxene/liquid trace element partitioning in natural  
1162 trachyte–trachyphonolite systems: insights from Campi Flegrei (south-  
1163 ern Italy). *Contributions to Mineralogy and Petrology* 158, 337–356.  
1164 doi:10.1007/s00410-009-0386-5.

- 1165 Foley, S.F., Prelevic, D., Rehfeldt, T., Jacob, D.E., 2013. Minor and  
1166 trace elements in olivines as probes into early igneous and mantle  
1167 melting processes. *Earth and Planetary Science Letters* 363, 181–191.  
1168 doi:10.1016/j.epsl.2012.11.025.
- 1169 Francis, D., Minarik, W., 2008. Aluminum-dependent trace element parti-  
1170 tioning in clinopyroxene. *Contributions to Mineralogy and Petrology* 156,  
1171 439–451. doi:10.1007/s00410-008-0295-z.
- 1172 Gaetani, G.A., 2004. The influence of melt structure on trace element par-  
1173 titioning near the peridotite solidus. *Contributions to Mineralogy and*  
1174 *Petrology* 147, 511–527. doi:10.1007/s00410-004-0575-1.
- 1175 Gaetani, G.A., Grove, T.L., 1995. Partitioning of rare earth elements between  
1176 clinopyroxene and silicate melt: Crystal-chemical controls. *Geochimica et*  
1177 *Cosmochimica Acta* 59, 1951–1962. doi:10.1016/0016-7037(95)00119-0.
- 1178 Gaillard, F., Scaillet, B., Pichavant, M., 2002. Kinetics of iron oxidation-  
1179 reduction in hydrous silicic melts. *American Mineralogist* 87, 829–837.  
1180 doi:10.2138/am-2002-0704.
- 1181 Giehl, C., Marks, M., Nowak, M., 2013. Phase relations and liquid lines  
1182 of descent of an iron-rich peralkaline phonolitic melt: an experimen-  
1183 tal study. *Contributions to Mineralogy and Petrology* 165, 283–304.  
1184 doi:10.1007/s00410-012-0809-6.
- 1185 Giordano, D., Nichols, A., Dingwell, D., 2005. Glass transition temperatures  
1186 of natural hydrous melts: a relationship with shear viscosity and impli-

- 1187 cations for the welding process. *Journal of Volcanology and Geothermal*  
1188 Research 142, 105–118. doi:10.1016/j.jvolgeores.2004.10.015.
- 1189 Girnis, A.V., Bulatov, V.K., Brey, G.P., Gerdes, A., Höfer, H.E., 2013. Trace  
1190 element partitioning between mantle minerals and silico-carbonate melts  
1191 at 6–12 GPa and applications to mantle metasomatism and kimberlite  
1192 genesis. *Lithos* 160–161, 183–200. doi:10.1016/j.lithos.2012.11.027.
- 1193 Goodenough, K.M., Schilling, J., Jonsson, E., Kalvig, P., Charles, N., Tuduri,  
1194 J., Deady, E.A., Sadeghi, M., Schiellerup, H., Müller, A., Bertrand, G.,  
1195 Arvanitidis, N., Eliopoulos, D.G., Shaw, R.A., Thrane, K., Keulen, N.,  
1196 2016. Europe's rare earth element resource potential: An overview of  
1197 REE metallogenetic provinces and their geodynamic setting. *Ore Geology  
1198 Reviews* 72, 838–856. doi:10.1016/j.oregeorev.2015.09.019.
- 1199 Grove, T.L., Baker, M.B., Kinzler, R.J., 1984. Coupled CaAl-NaSi dif-  
1200 fusion in plagioclase feldspar: Experiments and applications to cooling  
1201 rate speedometry. *Geochimica et Cosmochimica Acta* 48, 2113–2121.  
1202 doi:10.1016/0016-7037(84)90391-0.
- 1203 Guillou, H., Carracedo, J.C., Paris, R., Pérèz Torrado, F.J., 2004. Implica-  
1204 tions for the early shield-stage evolution of Tenerife from K/Ar ages and  
1205 magnetic stratigraphy. *Earth and Planetary Science Letters* 222, 599–614.  
1206 doi:10.1016/j.epsl.2004.03.012.
- 1207 Gurenko, A.A., Hoernle, K.A., Hauff, F., Schmincke, H.U., Han, D., Miura,  
1208 Y.N., Kaneoka, I., 2006. Major, trace element and NdSrPbOHeAr isotope  
1209 signatures of shield stage lavas from the central and western Canary Is-

- 1210 lands: Insights into mantle and crustal processes. *Chemical Geology* 233,  
1211 75–112. doi:10.1016/j.chemgeo.2006.02.016.
- 1212 Hanchar, J.M., Finch, R.J., Hoskin, P.W.O., Watson, E.B., Cheren-  
1213 niak, D.J., Mariano, A.N., 2001. Rare earth elements in synthetic  
1214 zircon: Part 1. Synthesis, and rare earth element and phospho-  
1215 rus doping. *American Mineralogist* 86, 667–680. doi:10.1130/0091-  
1216 7613(1990)018:0757:CTOGAS;2.3.CO;2.
- 1217 Hazen, R.M., Finger, L.W., 1979. Bulk modulus-volume relationship for  
1218 cation-anion polyhedra. *Journal of Geophysical Research: Solid Earth* 84,  
1219 6723–6728. doi:10.1029/JB084iB12p06723.
- 1220 Hill, E., Blundy, J.D., Wood, B.J., 2011. Clinopyroxene-melt trace ele-  
1221 ment partitioning and the development of a predictive model for HFSE  
1222 and Sc. *Contributions to Mineralogy and Petrology* 161, 423–438.  
1223 doi:10.1007/s00410-010-0540-0.
- 1224 Hill, E., Wood, B.J., Blundy, J.D., 2000. The effect of Ca-Tschermaks com-  
1225 ponent on trace element partitioning between clinopyroxene and silicate  
1226 melt. *Lithos* 53, 203–215. doi:10.1016/S0024-4937(00)00025-6.
- 1227 Huang, F., Lundstrom, C.C., McDonough, W.F., 2006. Effect of melt  
1228 structure on trace-element partitioning between clinopyroxene and sili-  
1229 cic, alkaline, aluminous melts. *American Mineralogist* 91, 1385–1400.  
1230 doi:10.2138/am.2006.1909.
- 1231 Jugo, P.J., Wilke, M., Botcharnikov, R.E., 2010. Sulfur K-edge XANES anal-  
1232 ysis of natural and synthetic basaltic glasses: Implications for S speciation

- 1233 and S content as function of oxygen fugacity. *Geochimica et Cosmochimica*  
1234 *Acta* 74, 5926–5938. doi:10.1016/j.gca.2010.07.022.
- 1235 Kennedy, A.K., Lofgren, G.E., Wasserburg, G.J., 1993. An experimental  
1236 study of trace element partitioning between olivine, orthopyroxene and  
1237 melt in chondrules: equilibrium values and kinetic effects. *Earth and Plan-  
1238 etary Science Letters* 115, 177–195. doi:10.1016/0012-821X(93)90221-T.
- 1239 Kogarko, L.N., 1990. Ore-forming potential of alkaline magmas. *Lithos* 26,  
1240 167–175. doi:10.1016/0024-4937(90)90046-4.
- 1241 Kovalenko, V.I., Hervig, R.L., Sheridan, M.F., 1988. Ion microprobe anal-  
1242 yses of trace elements in anorthoclase, hedenbergite, aenigmatite, quartz,  
1243 apatite and glass in pantellerite: evidence for high water contents in pan-  
1244 tellerite melt. *American Mineralogist* 73, 1038–1045.
- 1245 Kress, V.C., Carmichael, I.S.E., 1991. The compressibility of silicate liquids  
1246 containing Fe<sub>2</sub>O<sub>3</sub> and the effect of composition, temperature, oxygen fu-  
1247 gacity and pressure on their redox states. *Contributions to Mineralogy and*  
1248 *Petrology* 108, 82–92. doi:10.1007/BF00307328.
- 1249 Kumazawa, M., 1969. The elastic constants of single-crystal or-  
1250 thopyroxene. *Journal of Geophysical Research* 74, 5973–5980.  
1251 doi:10.1029/JB074i025p05973.
- 1252 Larsen, L.M., 1979. Distribution of REE and other trace elements between  
1253 phenocrysts and peralkaline undersaturated magmas, exemplified by rocks  
1254 from the Gardar igneous province, south Greenland. *Lithos* 12, 303–315.  
1255 doi:10.1016/0024-4937(79)90022-7.

- 1256 Law, K.M., Blundy, J.D., Wood, B.J., Ragnarsdottir, K.V., 2000. Trace ele-  
1257       ment partitioning between wollastonite and silicate-carbonate melt. Min-  
1258       eralogical Magazine 64, 651–661. doi:10.1180/002646100549670.
- 1259 Le Bas, M.J., Le Maitre, R.W., Streckeisen, A., Zanettin, B., 1986. A Chem-  
1260       ical Classification of Volcanic Rocks Based on the Total Alkali-Silica Dia-  
1261       gram. Journal of Petrology 27, 745–750. doi:10.1093/petrology/27.3.745.
- 1262 Liang, Y., Richter, F.M., Watson, E.B., 1994. Convection in multicom-  
1263       ponent silicate melts driven by coupled diffusion. Nature 369, 390–392.  
1264       doi:10.1038/369390a0.
- 1265 Linnen, R.L., Keppeler, H., 1997. Columbite solubility in granitic melts:  
1266       consequences for the enrichment and fractionation of Nb and Ta in the  
1267       Earth's crust. Contributions to Mineralogy and Petrology 128, 213–227.  
1268       doi:10.1007/s004100050304.
- 1269 Lofgren, G., 1989. Dynamic crystallization of chondrule melts of porphyritic  
1270       olivine composition: Textures experimental and natural. Geochimica et  
1271       Cosmochimica Acta 53, 461–470. doi:10.1016/0016-7037(89)90397-9.
- 1272 Lofgren, G.E., Huss, G.R., Wasserburg, G.J., 2006. An experimental study  
1273       of trace-element partitioning between Ti-Al-clinopyroxene and melt: Equi-  
1274       librium and kinetic effects including sector zoning. American Mineralogist  
1275       91, 1596–1606. doi:10.2138/am.2006.2108.
- 1276 Lu, F., Anderson, A.T., Davis, A.M., 1995. Diffusional gradients at the crys-  
1277       tal / melt interface and their effect on the compositions of melt inclusions.  
1278       The Journal of Geology 103, 591–597.

- 1279 Lundstrom, C.C., Shaw, H.F., Ryerson, F.J., Phinney, D.L., Gill, J.B.,  
1280 Williams, Q., 1994. Compositional controls on the partitioning of U, Th,  
1281 Ba, Pb, Sr and Zr between clinopyroxene and haplobasaltic melts: impli-  
1282 cations for uranium series disequilibria in basalts. *Earth and Planetary*  
1283 *Science Letters* 128, 407–423. doi:10.1016/0012-821X(94)90159-7.
- 1284 Mahood, G.A., Stimac, J.A., 1990. Trace-element partitioning in pantel-  
1285 lerites and trachytes. *Geochimica et Cosmochimica Acta* 54, 2257–2276.  
1286 doi:10.1016/0016-7037(90)90050-U.
- 1287 Marks, M., Halama, R., Wenzel, T., Markl, G., 2004. Trace element vari-  
1288 ations in clinopyroxene and amphibole from alkaline to peralkaline syen-  
1289 ites and granites: implications for mineral-melt trace-element partitioning.  
1290 *Chemical Geology* 211, 185–215. doi:10.1016/j.chemgeo.2004.06.032.
- 1291 Marks, M., Markl, G., 2001. Fractionation and assimilation processes in the  
1292 alkaline augite syenite unit of the Ilímaussaq intrusion, south Greenland,  
1293 as deduced from phase equilibria. *Journal of Petrology* 42, 1947–1969.  
1294 doi:10.1093/petrology/42.10.1947.
- 1295 Marks, M., Markl, G., 2003. Ilímaussaq en miniature': closed-system frac-  
1296 tionation in an agpaitic dyke rock from the Gardar Province, South Green-  
1297 land (contribution to the mineralogy of Ilímaussaq no. 117). *Mineralogical*  
1298 *Magazine* 67, 893–919. doi:10.1180/0026461036750150.
- 1299 Marks, M.A., Markl, G., 2017. A global review on agpaitic rocks. *Earth-*  
1300 *Science Reviews* 173, 229–258. doi:10.1016/j.earscirev.2017.06.002.

- 1301 Marks, M.A.W., Hettmann, K., Schilling, J., Frost, B.R., Markl, G., 2011.  
1302 The mineralogical diversity of alkaline igneous rocks: Critical factors for  
1303 the transition from miaskitic to agpaitic phase assemblages. *Journal of*  
1304 *Petrology* 52, 439–455. doi:10.1093/petrology/egq086.
- 1305 Möller, V., Williams-Jones, A.E., 2016. Petrogenesis of the Necha-  
1306 lacho Layered Suite, Canada: magmatic evolution of a REE-Nb-  
1307 rich nepheline syenite intrusion. *Journal of Petrology* 57, 229–276.  
1308 doi:10.1093/petrology/egw003.
- 1309 Mollo, S., Blundy, J.D., Giacomoni, P., Nazzari, M., Scarlato, P., Coltorti,  
1310 M., Langone, A., Andronico, D., 2017. Clinopyroxene-melt element par-  
1311 titioning during interaction between trachybasaltic magma and siliceous  
1312 crust: Clues from quartzite enclaves at Mt. Etna volcano. *Lithos* 284-285,  
1313 447–461. doi:10.1016/j.lithos.2017.05.003.
- 1314 Mollo, S., Blundy, J.D., Iezzi, G., Scarlato, P., Langone, A., 2013. The  
1315 partitioning of trace elements between clinopyroxene and trachybasaltic  
1316 melt during rapid cooling and crystal growth. *Contributions to Mineralogy*  
1317 and *Petrology* 166, 1633–1654. doi:10.1007/s00410-013-0946-6.
- 1318 Mollo, S., Forni, F., Bachmann, O., Blundy, J.D., De Astis, G., Scarlato,  
1319 P., 2016. Trace element partitioning between clinopyroxene and trachy-  
1320 phonolitic melts: A case study from the Campanian Ignimbrite (Campi  
1321 Flegrei, Italy). *Lithos* 252253, 160–172. doi:10.1016/j.lithos.2016.02.024.
- 1322 Moore, G., Vennemann, T., Carmichael, I.S.E., 1998. An empirical model

- 1323 for the solubility of H<sub>2</sub>O in magmas to 3 kilobars. American Mineralogist  
1324 83, 36–42. doi:10.1016/0012-821X(73)90129-5.
- 1325 Morimoto, N., 1989. Nomenclature of pyroxenes. Mineralogical Journal 14,  
1326 198–221. doi:10.2465/minerj.14.198.
- 1327 Mungall, J., Brenan, J., 2014. Partitioning of platinum-group elements and  
1328 Au between sulfide liquid and basalt and the origins of mantle-crust frac-  
1329 tionation of the chalcophile elements. Geochimica et Cosmochimica Acta  
1330 125, 265–289. doi:10.1016/j.gca.2013.10.002.
- 1331 Mysen, B.O., Virgo, D., Seifert, F.A., 1982. The structure of silicate melts:  
1332 Implications for chemical and physical properties of natural magma. Re-  
1333 views of Geophysics 20, 353–383. doi:10.1029/RG020i003p00353.
- 1334 Mysen, B.O., Virgo, D., Seifert, F.A., 1985. Relationships between properties  
1335 and structure of aluminosilicate melts. American Mineralogist 70, 88–105.  
1336 doi:10.1007/BF00413348.
- 1337 Niu, Y., 2004. Bulk-rock major and trace element compositions of abyssal  
1338 peridotites: Implications for mantle melting, melt extraction and post-  
1339 melting processes beneath Mid-Ocean ridges. Journal of Petrology 45,  
1340 2423–2458. doi:10.1093/petrology/egh068.
- 1341 Olin, P.H., Wolff, J.A., 2010. Rare earth and high field strength element par-  
1342 titioning between iron-rich clinopyroxenes and felsic liquids. Contributions  
1343 to Mineralogy and Petrology 160, 761–775. doi:10.1007/s00410-010-0506-2.
- 1344 Onuma, N., Higuchi, H., Wakita, H., Nagasawa, H., 1968. Trace element

- partition between two pyroxenes and the host lava. *Earth and Planetary Science Letters* 5, 47–51. doi:10.1016/S0012-821X(68)80010-X.
- Paton, C., Hellstrom, J., Paul, B., Woodhead, J., Hergt, J., 2011. Iolite: Freeware for the visualisation and processing of mass spectrometric data. *Journal of Analytical Atomic Spectrometry* 26, 2508–2518. doi:10.1039/C1JA10172B.
- Peters, S.T., Troll, V.R., Weis, F.A., Dallai, L., Chadwick, J.P., Schulz, B., 2017. Amphibole megacrysts as a probe into the deep plumbing system of Merapi volcano, Central Java, Indonesia. *Contributions to Mineralogy and Petrology* 172, 1–20. doi:10.1007/s00410-017-1338-0.
- Prowatke, S., Klemme, S., 2005. Effect of melt composition on the partitioning of trace elements between titanite and silicate melt. *Geochimica et Cosmochimica Acta* 69, 695–709. doi:10.1016/j.gca.2004.06.037.
- Putirka, K.D., 2008. Thermometers and Barometers for Volcanic Systems. *Reviews in Mineralogy and Geochemistry* 69, 61–120. doi:10.2138/rmg.2008.69.3.
- Rapp, R.P., Watson, E.B., 1986. Monazite solubility and dissolution kinetics: implications for the thorium and light rare earth chemistry of felsic magmas. *Contributions to Mineralogy and Petrology* 94, 304–316. doi:10.1007/BF00371439.
- Rasband, W., 2016. ImageJ, U.S. National Institutes of Health, Bethesda, Maryland, USA.

- 1367 Redhammer, G.J., Amthauer, G., Roth, G., Tippelt, G., Lotter-  
1368 moser, W., 2006. Single-crystal X-ray diffraction and temperature  
1369 dependent  $^{57}\text{Fe}$  Mössbauer spectroscopy on the hedenbergite-aegirine  
1370  $(\text{Ca},\text{Na})(\text{Fe}^{2+},\text{Fe}^{3+})\text{Si}_2\text{O}_6$  solid solution. American Mineralogist 91,  
1371 1271–1292. doi:10.2138/am.2006.2173.
- 1372 Reguir, E.P., Chakhmouradian, A.R., Pisiak, L., Halden, N.M., Yang, P.,  
1373 Xu, C., Kynický, J., Couëslan, C.G., 2012. Trace-element composition  
1374 and zoning in clinopyroxene- and amphibole-group minerals: Implications  
1375 for element partitioning and evolution of carbonatites. Lithos 128, 27–45.  
1376 doi:10.1016/j.lithos.2011.10.003.
- 1377 Rubatto, D., Hermann, J., 2007. Experimental zircon/melt and  
1378 zircon/garnet trace element partitioning and implications for the  
1379 geochronology of crustal rocks. Chemical Geology 241, 38–61.  
1380 doi:10.1016/j.chemgeo.2007.01.027.
- 1381 Schmidt, B.C., Behrens, H., 2008. Water solubility in phonolite melts: Influ-  
1382 ence of melt composition and temperature. Chemical Geology 256, 259–  
1383 268. doi:10.1016/j.chemgeo.2008.06.043.
- 1384 Schmidt, K.H., Bottazzi, P., Vannucci, R., Mengel, K., 1999. Trace element  
1385 partitioning between phlogopite, clinopyroxene and leucite lamproite melt.  
1386 Earth and Planetary Science Letters 168, 287–299. doi:10.1016/S0012-  
1387 821X(99)00056-4.
- 1388 Schmidt, M.W., Connolly, J.A.D., Günther, D., Bogaerts, M., 2006. Element

- partitioning: The role of melt structure and composition. *Science* 312, 1646–1650. doi:10.1126/science.1126690.
- Severs, M.J., Beard, J.S., Fedele, L., Hanchar, J.M., Mutchler, S.R., Bodnar, R.J., 2009. Partitioning behavior of trace elements between dacitic melt and plagioclase, orthopyroxene, and clinopyroxene based on laser ablation ICPMS analysis of silicate melt inclusions. *Geochimica et Cosmochimica Acta* 73, 2123–2141. doi:10.1016/j.gca.2009.01.009.
- Shannon, R., 1976. Revised effective ionic radii and systematic studies of interatomic distances in halides and chalcogenides. *Acta Crystallographica Section A* 32, 751–767.
- Shea, T., Hammer, J.E., 2013. Kinetics of cooling- and decompression-induced crystallization in hydrous mafic-intermediate magmas. *Journal of Volcanology and Geothermal Research* 260, 127–145. doi:10.1016/j.jvolgeores.2013.04.018.
- Shearer, C.K., Larsen, L.M., 1994. Sector-zoned aegirine from the Ilimaussaq alkaline intrusion, South Greenland; implications for trace-element behavior in pyroxene. *American Mineralogist* 79, 340–352.
- Sjöqvist, A., Cornell, D., Andersen, T., Erambert, M., Ek, M., Leijd, M., 2013. Three compositional varieties of rare-earth element ore: Eudialyte-group minerals from the Norra Kärr alkaline complex, Southern Sweden. *Minerals* 3, 94–120. doi:10.3390/min3010094.
- Sørensen, H., 1992. Agpaitic nepheline syenites: a potential source of

- <sup>1411</sup> rare elements. *Applied Geochemistry* 7, 417–427. doi:10.1016/0883-  
<sup>1412</sup> 2927(92)90003-L.
- <sup>1413</sup> Spera, F.J., Bohrson, W.A., 2001. Energy-constrained open-system mag-  
<sup>1414</sup> matic processes I: General model and energy-constrained assimilation and  
<sup>1415</sup> fractional crystallization (EC-AFC) formulation. *Journal of Petrology* 42,  
<sup>1416</sup> 999–1018. doi:10.1093/petrology/42.5.999.
- <sup>1417</sup> Stevens, J., 1996. Applied multivariate analysis for the social sciences.  
<sup>1418</sup> Lawrence Erlbaum, Mahwah, NJ.
- <sup>1419</sup> Sun, C., Liang, Y., 2012. Distribution of REE between clinopyroxene and  
<sup>1420</sup> basaltic melt along a mantle adiabat: Effects of major element composi-  
<sup>1421</sup> tion, water, and temperature. *Contributions to Mineralogy and Petrology*  
<sup>1422</sup> 163, 807–823. doi:10.1007/s00410-011-0700-x.
- <sup>1423</sup> Thirlwall, M.F., Singer, B.S., Marriner, G.F., 2000. <sup>39</sup>Ar–<sup>40</sup>Ar ages and  
<sup>1424</sup> geochemistry of the basaltic shield stage of Tenerife, Canary Islands,  
<sup>1425</sup> Spain. *Journal of Volcanology and Geothermal Research* 103, 247–297.  
<sup>1426</sup> doi:10.1016/S0377-0273(00)00227-4.
- <sup>1427</sup> Troll, V., Schmincke, H., 2002. Magma mixing and crustal recycling recorded  
<sup>1428</sup> in ternary feldspar from compositionally zoned peralkaline ignimbrite  
<sup>1429</sup> 'A', Gran Canaria, Canary Islands. *Journal of Petrology* 43, 243–270.  
<sup>1430</sup> doi:10.1093/petrology/43.2.243.
- <sup>1431</sup> Van Orman, J.A., Grove, T.L., Shimizu, N., 2001. Rare earth element diffu-  
<sup>1432</sup> sion in diopside: influence of temperature, pressure, and ionic radius, and

- 1433        an elastic model for diffusion in silicates. Contributions to Mineralogy and  
1434        Petrology 141, 687–703. doi:10.1007/s004100100269.
- 1435        Walker, D., Kirkpatrick, R.J., Longhi, J., Hays, J.F., 1976. Crystallization  
1436        history of lunar picritic basalt sample 12002: Phase-equilibria and cooling-  
1437        rate studies. Bulletin of the Geological Society of America 87, 646–656.  
1438        doi:10.1130/0016-7606.
- 1439        Watson, E.B., 1979. Zircon saturation in felsic liquids: Experimental results  
1440        and applications to trace element geochemistry. Contributions to Miner-  
1441        alogy and Petrology 70, 407–419. doi:10.1007/BF00371047.
- 1442        Weidner, D.J., Vaughan, M.T., 1982. Elasticity of pyroxenes: Effects of  
1443        composition versus crystal structure. Journal of Geophysical Research 87,  
1444        9349–9353.
- 1445        Wiesmaier, S., Troll, V.R., Carracedo, J.C., Ellam, R.M., Bindeman, I.,  
1446        Wolff, J.A., 2012. Bimodality of lavas in the Teide–Pico Viejo Succession  
1447        in Tenerife—the role of crustal melting in the origin of recent phonolites.  
1448        Journal of Petrology 53, 2465–2495. doi:10.1093/petrology/egs056.
- 1449        Wood, B.J., Blundy, J.D., 1997. A predictive model for rare earth  
1450        element partitioning between clinopyroxene and anhydrous silicate  
1451        melt. Contributions to Mineralogy and Petrology 129, 166–181.  
1452        doi:10.1007/s004100050330.
- 1453        Wood, B.J., Blundy, J.D., 2001. The effect of cation charge on crystal–melt  
1454        partitioning of trace elements. Earth and Planetary Science Letters 188,  
1455        59–71. doi:10.1016/S0012-821X(01)00294-1.

- 1456 Wood, B.J., Blundy, J.D., 2003. Trace element partitioning under crustal  
1457 and uppermost mantle conditions: The influences of ionic radius, cation  
1458 charge, pressure, and temperature, in: Carlson, R.W. (Ed.), *The Mantle*  
1459 and Core: Treatise on Geochemistry. Elsevier. volume 2. chapter 2.09, pp.  
1460 395–424. doi:10.1016/B0-08-043751-6/02009-0.
- 1461 Wood, B.J., Blundy, J.D., 2014. Trace element partitioning: The influences  
1462 of ionic radius, cation charge, pressure, and temperature, in: Carlson,  
1463 R.W. (Ed.), *The Mantle and Core: Treatise on Geochemistry: Second Edi-*  
1464 *tion*. Elsevier. chapter 3.11, pp. 421–445. doi:10.1016/B978-0-08-095975-  
1465 7.00206-0.
- 1466 Wood, B.J., Trigila, R., 2001. Experimental determination of aluminous  
1467 clinopyroxene–melt partition coefficients for potassic liquids, with applica-  
1468 tion to the evolution of the Roman province potassic magmas. *Chemical*  
1469 *Geology* 172, 213–223. doi:10.1016/S0009-2541(00)00259-X.
- 1470 Workman, R.K., Hart, S.R., 2005. Major and trace element composition of  
1471 the depleted MORB mantle (DMM). *Earth and Planetary Science Letters*  
1472 231, 53–72. doi:10.1016/j.epsl.2004.12.005.
- 1473 Wörner, G., Beusen, J.M., Duchateau, N., Gijbels, R., Schmincke, H.U.,  
1474 1983. Trace element abundances and mineral/melt distribution coefficients  
1475 in phonolites from the Laacher See volcano (Germany). *Contributions to*  
1476 *Mineralogy and Petrology* 84, 152–173. doi:10.1007/BF00371282.
- 1477 Xu, C., Kynicky, J., Chakhmouradian, A.R., Campbell, I.H., Allen, C.M.,  
1478 2010. Trace-element modeling of the magmatic evolution of rare-earth-rich

- 1479 carbonatite from the Miaoya deposit, Central China. *Lithos* 118, 145–155.  
1480 doi:10.1016/j.lithos.2010.04.003.
- 1481 Yang, L., van Hinsberg, V.J., Samson, I.M., 2018. A new method to decon-  
1482 volute binary mixture in LA-ICP-MS analyses to quantify the composition  
1483 of phases smaller than the laser spot size. *JAAS* .
- 1484 Yao, L., Sun, C., Liang, Y., 2012. A parameterized model for REE distri-  
1485 bution between low-Ca pyroxene and basaltic melts with applications to  
1486 REE partitioning in low-Ca pyroxene along a mantle adiabat and dur-  
1487 ing pyroxenite-derived melt and peridotite interaction. *Contributions to  
1488 Mineralogy and Petrology* 164, 261–280. doi:10.1007/s00410-012-0737-5.
- 1489 Zhang, Y., Ni, H., Chen, Y., 2010. Diffusion data in silicate melts. *Reviews  
1490 in Mineralogy and Geochemistry* 72, 311–408. doi:10.2138/rmg.2010.72.8.

<sup>1491</sup> **6. Tables**

Table 1: Major-element composition (in wt%) of starting materials for the internally heated pressure vessel experiments. The totals are calculated with all iron as FeO.

*Dry starting glass compositions calculated from masses of reagents added [wt%]*

Composition	SiO <sub>2</sub>	TiO <sub>2</sub>	Al <sub>2</sub> O <sub>3</sub>	FeOT	MgO	CaO	Na <sub>2</sub> O	K <sub>2</sub> O	Total	(Na+K)/Al
L4	57.48	1.50	19.00	5.89	1.61	3.21	7.33	3.98	100.00	0.861
L5	61.24	0.68	19.51	3.77	0.43	0.91	8.63	4.84	100.00	0.996
M3	52.67	2.27	18.13	7.86	2.75	5.40	7.19	3.73	100.00	0.875
M4	56.35	1.47	18.63	5.77	1.58	3.15	8.48	4.57	100.00	1.014
M5	60.04	0.66	19.13	3.69	0.42	0.89	9.76	5.41	100.00	1.145
H4	54.80	1.43	18.12	5.62	1.54	3.06	10.07	5.38	100.00	1.236
H5	58.38	0.65	18.60	3.59	0.41	0.86	11.31	6.20	100.00	1.362

*Water saturated glass compositions from superliquidus experiments (EPMA) [wt%]*

L5	57.46	0.643	16.59	2.363	0.404	0.985	7.840	4.462	90.75	1.069
s.d. (n = 8)	0.299	0.087	0.210	0.059	0.035	0.050	0.175	0.132	0.351	0.017
rsd	0.52%	13.58%	1.26%	2.51%	8.70%	5.09%	2.23%	2.97%	0.39%	1.57%
H5	55.58	0.612	16.21	2.568	0.422	0.906	10.77	5.732	92.80	1.476
s.d. (n = 13)	0.327	0.057	0.221	0.113	0.044	0.049	0.205	0.154	0.417	0.028
rsd	0.59%	9.33%	1.36%	4.41%	10.44%	5.40%	1.90%	2.69%	0.45%	1.87%

Table 2: Summary of run conditions and run products for the internally-heated pressure vessel experiments.

Experiment	Setup	Pressure [bar]	Cooling ramp				(after ramp) [h,m]	Run products
			Rate °C /min	Cycle +10°C	TE-1/TE-3 [°C ]	TE-2 (spl) [°C ]		
L4 <sub>3</sub>	IHPV RQ (f)	2038	1	Y	825	828	44h50m	Cpx + Ox + Ttn + Melt
L5 <sub>3</sub>	IHPV RQ (f)	2038	1	Y	825	828	44h50m	Cpx + Ox + Melt
M3 <sub>2</sub>	IHPV RQ	2020	1	Y	796/795	799	47h	Cpx + Ox + Bt + Melt
M4 <sub>4</sub>	IHPV RQ	2020	1	Y	796/795	799	47h	Cpx + Ox + Bt + Melt
M5	IHPV	2000	-	-	800	799	47h55m	Cpx + Bt + Fsp + Melt
M5 <sub>2</sub>	IHPV RQ	2000	-	-	700	689	45h45m	Cpx + Bt + Fsp + Melt
H4 <sub>2</sub>	IHPV	2000	-	-	800	799	47h55m	Cpx + Ttn + Melt
H5 <sub>2</sub>	IHPV RQ	2000	-	-	700	689	45h45m	Cpx + Bt + Fsp + Melt
H5 <sub>3</sub>	IHPV RQ	2020	-	-	651/649	648	46h15m	Cpx + Bt + Fsp + Melt
NLS-9	IHPV RQ	2020	1	Y	651/649	648	46h15m	Cpx + Ox + Melt
NLS-9 <sub>2</sub> HM	IHPV RQ**	2000	1	Y	650	655	42h	Cpx + Ox + Fsp + Melt

(f) indicates failure of the rapid quench apparatus; \*\* indicates use of a haematite double capsule, for run conditions at the haematite-magnetite  $f\text{O}_2$  buffer (Eugster and Wones, 1962). Cpx = clinopyroxene; Ox = spinel oxide; Ttn = titanite; Bt = biotite; Fsp = sanidine feldspar.

Table 3: Representative major-element compositions of clinopyroxene and melt for the performed internally heated pressure vessel experiments and Canary Islands phenocryst–glass pairs.

<i>Pyroxene</i>	L4 <sub>3</sub>	M3 <sub>2</sub>	M5 <sub>2</sub>	H5 <sub>3</sub>	NLS-9	NLS-9 <sub>2</sub> HM	16-07 LMB	17-12 M. Samara	17-14 UMB-II	21-30 PV 2 ka
SiO <sub>2</sub>	44.70	40.73	47.31	46.95	50.73	51.90	52.43	51.77	51.81	52.50
TiO <sub>2</sub>	3.07	4.57	3.17	4.47	0.10	0.10	0.80	0.78	0.74	0.75
Al <sub>2</sub> O <sub>3</sub>	5.23	9.26	3.08	3.10	2.46	2.96	1.33	1.24	1.27	1.22
FeO	13.31	11.72	18.84	16.95	28.14	28.61	9.71	9.62	10.51	10.02
MnO	0.01	0.01	0.01	0.00	0.25	0.17	0.78	0.84	0.91	0.81
MgO	9.09	9.28	5.55	6.05	0.05	0.07	12.30	12.64	12.07	11.88
CaO	19.49	22.17	16.11	15.29	5.88	3.14	21.90	21.76	21.52	22.02
Na <sub>2</sub> O	2.27	1.01	4.34	4.97	9.86	11.45	1.18	1.17	1.38	1.19
K <sub>2</sub> O	0.09	0.03	0.08	0.07	0.04	0.04	0.02	0.03	0.00	0.02
Total	97.25	98.78	98.49	97.85	97.49	98.45	100.44	99.85	100.22	100.42
<i>Glass</i>										
SiO <sub>2</sub>	58.79	57.29	57.45	54.91	58.17	58.14	60.38	55.10	59.08	60.04
TiO <sub>2</sub>	0.35	0.27	0.23	0.62	0.00	0.00	0.64	1.73	0.66	0.66
Al <sub>2</sub> O <sub>3</sub>	17.35	19.14	16.69	16.06	18.55	19.41	19.96	18.30	19.68	19.79
Fe <sub>2</sub> O <sub>3</sub> (T)	2.35	1.35	1.01	3.16	1.67	1.91	3.65	7.22	4.02	3.96
FeO(T)	2.12	1.22	0.91	2.84	1.50	1.72	3.28	6.49	3.62	3.56
MnO	0.02	0.00	-	0.01	0.06	0.04	0.14	0.23	0.22	0.20
MgO	0.20	0.13	0.15	0.35	0.00	0.00	0.39	1.84	0.32	0.35
CaO	0.55	0.95	0.24	0.84	0.23	0.23	0.76	4.10	0.77	0.74
Na <sub>2</sub> O	7.17	7.32	9.08	8.88	11.12	9.80	9.00	7.26	9.76	9.05
K <sub>2</sub> O	4.68	4.10	4.68	5.30	1.51	2.51	5.41	4.09	5.45	5.57
Total	91.23	90.41	89.43	89.81	91.15	91.85	99.95	99.13	99.56	99.95
(Na+K)/Al	0.97	0.86	1.15	1.27	1.07	0.97	1.01	1.12	1.09	1.09

Table 4: Pyroxene-melt trace-element-partition coefficients for representative experiments and a natural phenocryst-glass pair.

-	L4 <sub>3</sub>		M3 <sub>2</sub>		M5 <sub>2</sub>		H5 <sub>3</sub>		NLS-9		NLS-9 <sub>2</sub> HM		16-07-px4 LMB	
	D	$\sigma$	D	$\sigma$	D	$\sigma$	D	$\sigma$	D	$\sigma$	D	$\sigma$	D	$\sigma$
Li	0.250	0.016	0.126	0.009	0.419	0.034	0.427	0.024	0.274	0.029	0.251	0.025	0.157	0.021
Ga	0.364	0.022	0.567	0.020	0.190	0.022	-	-	-	-	-	-	0.216	0.020
Rb	0.005	0.002	0.018	0.003	0.010	0.006	0.013	0.002	0.026	0.015	-	-	0.000	0.000
Sr	0.828	0.045	0.282	0.024	1.433	0.111	0.997	0.091	0.321	0.045	0.269	0.111	0.732	0.293
Y	5.577	0.302	13.784	1.949	1.814	0.236	1.102	0.060	0.482	0.048	0.713	0.070	2.183	0.232
Zr	1.699	0.082	2.537	0.222	1.361	0.089	1.164	0.083	2.102	0.196	3.895	0.482	0.434	0.047
Nb	0.126	0.085	0.889	0.258	0.554	0.280	1.688	0.196	2.382	0.294	9.642	4.015	0.0062	0.0004
Cs	0.019	0.003	0.019	0.003	0.014	0.006	0.010	0.002	-	-	0.023	0.017	0.001	0.001
Ba	0.0364	0.0087	0.0373	0.0152	0.0388	0.0261	0.0288	0.0091	-	-	-	-	0.00004	0.00004
La	4.787	0.646	2.591	0.240	4.658	0.962	3.049	0.132	0.410	0.037	0.542	0.043	0.769	0.071
Ce	7.199	0.756	6.229	0.646	5.199	1.073	3.190	0.129	0.377	0.028	0.547	0.061	1.591	0.120
Nd	16.105	1.537	28.430	4.210	6.454	1.630	3.759	0.147	0.579	0.054	0.925	0.114	2.632	0.155
Sm	17.843	1.414	47.245	7.699	5.215	1.293	3.113	0.137	0.388	0.070	0.767	0.182	3.522	0.421
Eu	16.403	1.341	53.195	8.181	4.743	1.132	2.900	0.133	0.275	0.082	0.682	0.192	3.372	0.196
Dy	9.027	0.537	27.082	3.925	2.619	0.460	1.521	0.073	0.329	0.057	0.388	0.088	2.798	0.220
Tm	4.773	0.261	9.067	0.903	2.937	0.279	1.567	0.097	1.330	0.145	2.860	0.890	1.846	0.182
Yb	4.797	0.249	7.015	0.600	3.937	0.296	2.281	0.152	2.564	0.346	8.004	3.116	1.978	0.186
Hf	2.385	0.162	3.556	0.472	1.802	0.118	1.141	0.123	2.443	0.275	3.702	0.479	0.769	0.065
Ta	0.496	0.152	2.3694	0.6244	0.6502	0.2545	1.5654	0.2337	2.1082	0.1764	3.6854	0.6561	0.0153	0.0013
Pb	0.079	0.017	0.0587	0.0152	0.1142	0.0349	0.0199	0.0130	0.0884	0.0280	0.0564	0.0536	0.0203	0.0040
Th	0.201	0.034	0.3565	0.0419	0.3172	0.0321	0.2892	0.0239	0.0798	0.0240	0.0709	0.0276	0.0040	0.0003
U	-	-	0.0512	0.0331	0.1261	0.0272	0.0196	0.0103	0.0460	0.0245	0.0834	0.0342	0.0022	0.0003

Table 5: Coefficients for prediction of lattice-strain parameters for clinopyroxene M1 and M2 sites from clinopyroxene composition, temperature and pressure. Fitted vs. predicted lattice-strain parameters and partition coefficients are in Figures 12–13 and full multiple linear regression reports are available as supplementary data file S4.

Model for $\text{Ln}D_0$ M2 site (n = 82)			Model for $\text{Ln}D_0$ , M1 site (n = 16)		
Parameter	Coefficient	$\sigma$	Parameter	Coefficient	$\sigma$
Intercept	4.52	0.91	Intercept	5	1
M1Ti	6.8	3	TAl	4	0.5
M1Al - M1Fe <sup>3+</sup>	1.6	0.6	M1Fe <sup>2+</sup>	2.6	0.9
M2Fe <sup>2+</sup>	-3.8	1.3	M2Na	-8	1
T [K]	-0.0035	0.0007	M2Ca	-3	2
TAl + TFe <sup>3+</sup>	2.6	0.8			
$R^2$		0.647			0.959

Model for $E_s$ , M2 site (n = 79)			Model for $E_s$ , M1 site (n = 18)		
Parameter	Coefficient	$\sigma$	Parameter	Coefficient	$\sigma$
Intercept	247	44	Intercept	-2322	298
M1Al	-424	144	T [K]	3.2	0.4
M1Mg	-285	102	P [GPa]	-408	145
M1Ti	-1145	378	M1Mg	-800	212
M2Mg	-306	115			
P [GPa]	37	12			
TAl + TFe <sup>3+</sup>	313	102			
XMg	336	102			
$R^2$		0.348			0.936

Model for $r_0$ , M2 site (n = 82)			Model for $r_0$ , M1 site (n = 16)		
Parameter	Coefficient	$\sigma$	Parameter	Coefficient	$\sigma$
Intercept	1.01	0.02	Intercept	0.79	0.03
M1Ti	0.16	0.05	P [GPa]	-0.017	0.005
M1Al-M1Fe <sup>3+</sup>	-0.03	0.01	M2Mg	-0.48	0.06
M2Ca	0.09	0.02	M1Fe <sup>3+</sup>	0.14	0.03
M2Na	0.14	0.02	M2Ca	-0.05	0.02
T [K]	-4.46E-05	1.22E-05			
$R^2$		0.846			0.987

1492 7. Supplementary figures

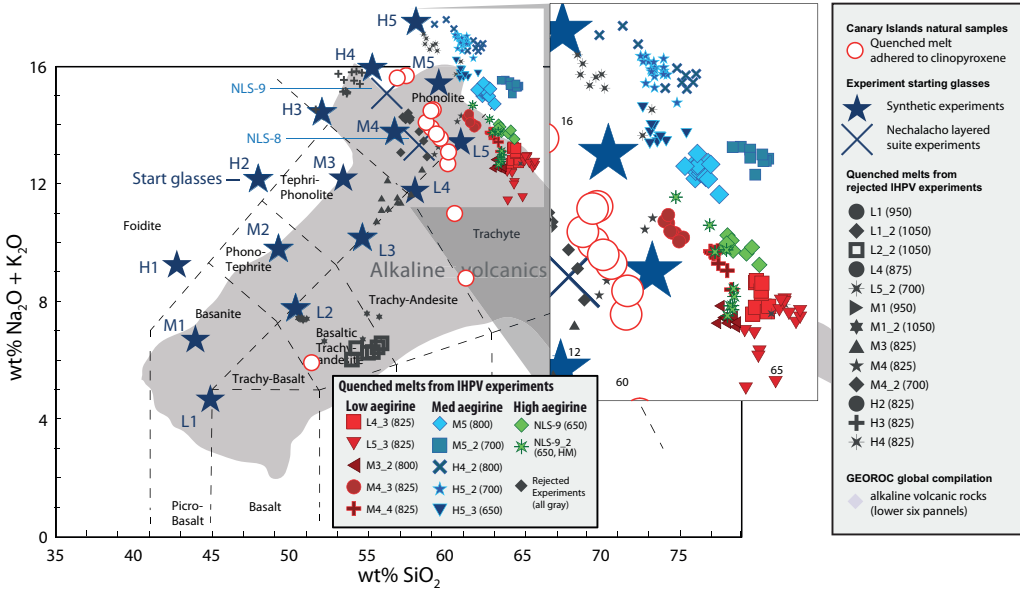


Figure S1: Total alkalies vs. silica diagram for glasses produced in internally heated pressure vessel experiments and adhered to Canary Islands clinopyroxene phenocrysts (Le Bas et al., 1986). Large stars indicate synthetic starting glass compositions as used in internally heated pressure vessel experiments (Table 1), whereas large crosses indicate the composition of powdered natural samples from the Nechalacho layered suite, NT, Canada that were used as starting materials for some experiments. The gray field indicates the compositional range expressed by alkaline volcanic provinces from around the world, sourced from the GEOROC database. Rejected experiments in dark gray are not discussed in the main text, and either did not produce clinopyroxene, produced crystals that were too small for analysis by LA-ICP-MS, or grew crystals during quench, hence preserving disequilibrium partitioning behaviour. Further diagrams showing major-element compositions for the quenched melts and the starting glasses are in Fig S2.

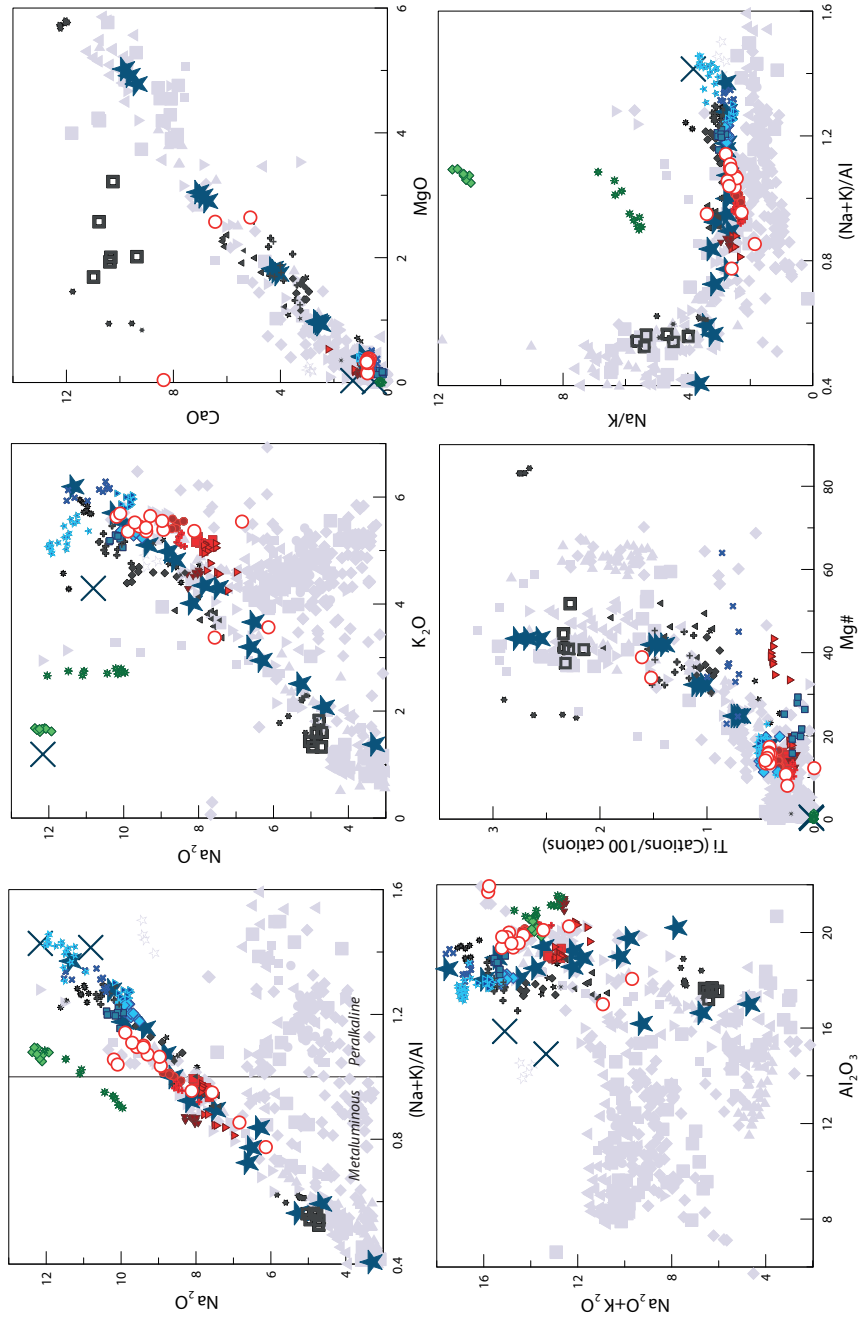


Figure S2: Major-element compositions for glass produced in the internally heated pressure vessel experiments and adhered to clinopyroxene phenocrysts from the Canary Islands. Symbols as in Fig. S1.

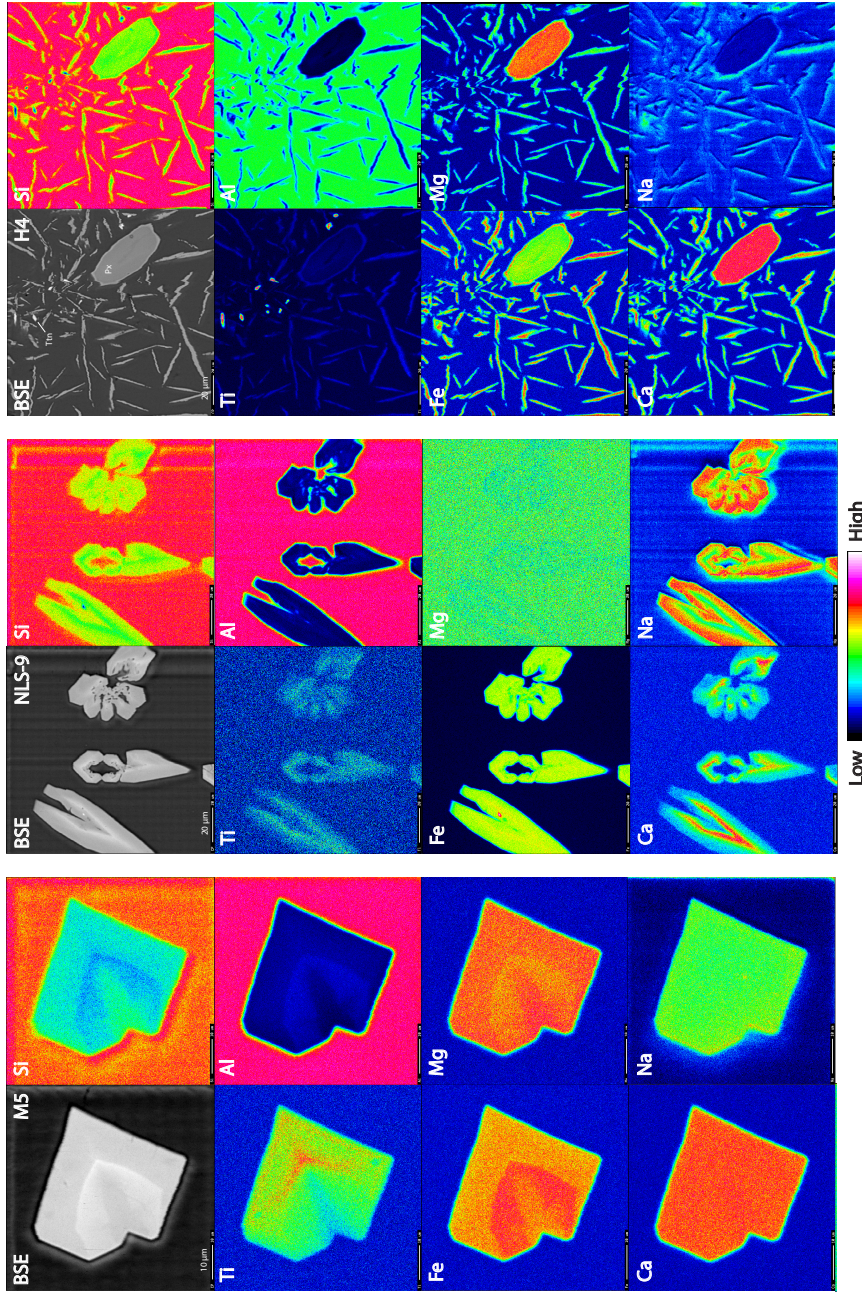


Figure S3: Element maps of clinopyroxene from internally heated pressure vessel experiments. M5 clinopyroxene have a sharp internal boundary that reflects feldspar saturation and are subtly zoned. NLS-9 clinopyroxene are more strongly zoned with swallowtail and hopper textures and rare inclusions of magnetite (cf. Walker et al., 1976; Lofgren, 1989; Shea and Hammer, 2013). H4 clinopyroxene ( $P_X$ ) display a bimodal crystal size distribution and occur with titanite (Tn). The bimodal crystal size distribution is due to a temperature perturbation during run, and renders this experiment unsuitable for this element partitioning study.

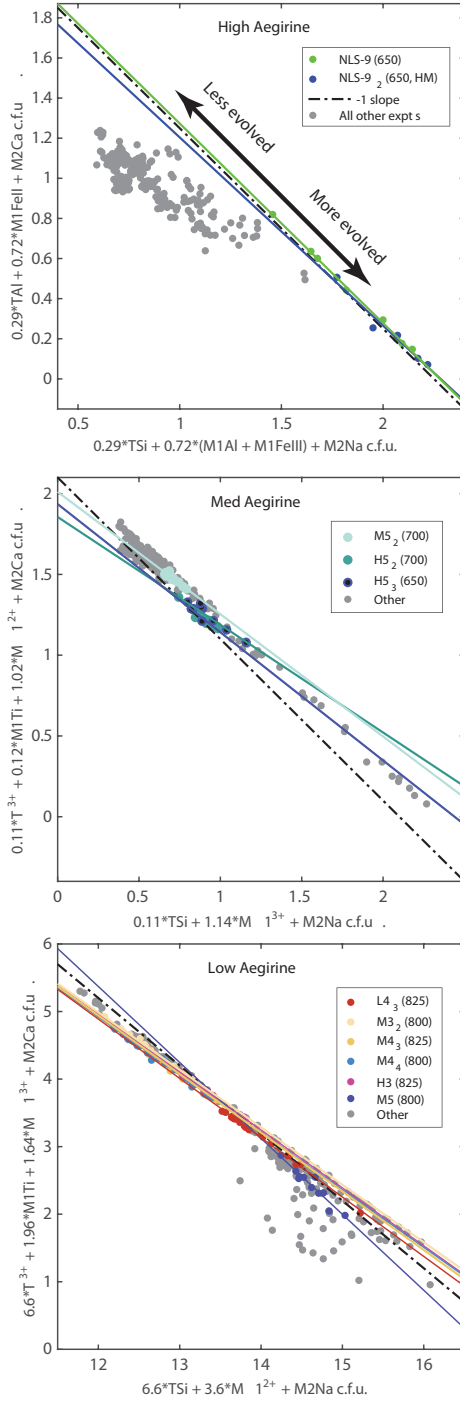


Figure S4: Major-element exchange mechanisms for (a) high, (b) medium and (c) low-aegirine clinopyroxene generated in internally heated pressure vessel experiments. Each individual plotted point represents an electron-microprobe analysis. Iron in the clinopyroxene was assigned to 2+ or 3+ valence following Droop (1987), then major-element cations were assigned to sites following Morimoto (1989, see supplement S5). Axes were defined by linear regressions between site-assigned major-element abundances, which have been checked for consistency in total site-occupancy and for charge.

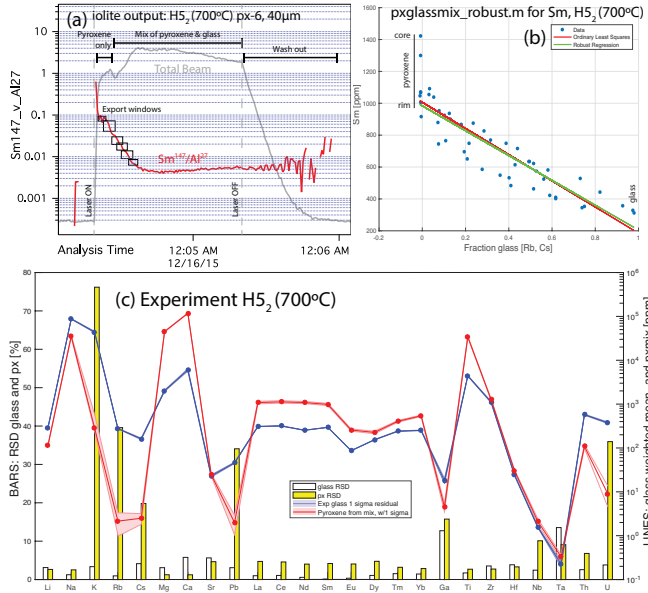


Figure S5: An example of the robust regression data reduction scheme for laser-ablation ICP-MS analyses of glass and clinopyroxene mixtures. (a) Time series of laser-ablation data, showing traces for Sm/Al (red) and total beam intensity (gray). The laser beam often ablated through the small clinopyroxene crystals, returning a mixed signal that was exported from the iolite data reduction software in short time windows as shown. Data were then normalised to the sum of major-element concentrations and mixes were deconvolved using a robust regression script written in MATLAB. (b) An example output diagram for the robust regression data reduction scheme. Clinopyroxene–glass mixing ratios were constrained by strongly incompatible elements Rb and Cs. For each element, a robust linear regression was defined between the fraction of glass in the mixture and element concentration. The intercept of this regression with zero glass returned the trace-element concentrations in the clinopyroxene. Uncertainty with this technique is typically below 10 % relative (median 9.3 % at the  $1\sigma$  level). In this example, the Sm-rich core of a zoned clinopyroxene crystal is effectively rejected during data processing, and the derived Sm concentration for the clinopyroxene is therefore closer to that of the clinopyroxene rims that are in equilibrium with the adjacent quenched melt. (c) A quality control diagram output from the MATLAB data reduction scheme showing the concentrations of various elements in the glass and clinopyroxene (lines) and the uncertainty on these concentrations expressed as a relative standard deviation (BARS). Derived partition coefficients ( $D_i$ ) are the mass concentration of element ' $i$ ' in clinopyroxene divided by that in the adjacent quenched melt. Residuals for the  $D_i$  values were calculated using uncertainties derived from the clinopyroxene and glass analyses to calculate minimum and maximum partition coefficients at the  $1\sigma$  level. These are reported in Table 4 and Supplement S1.

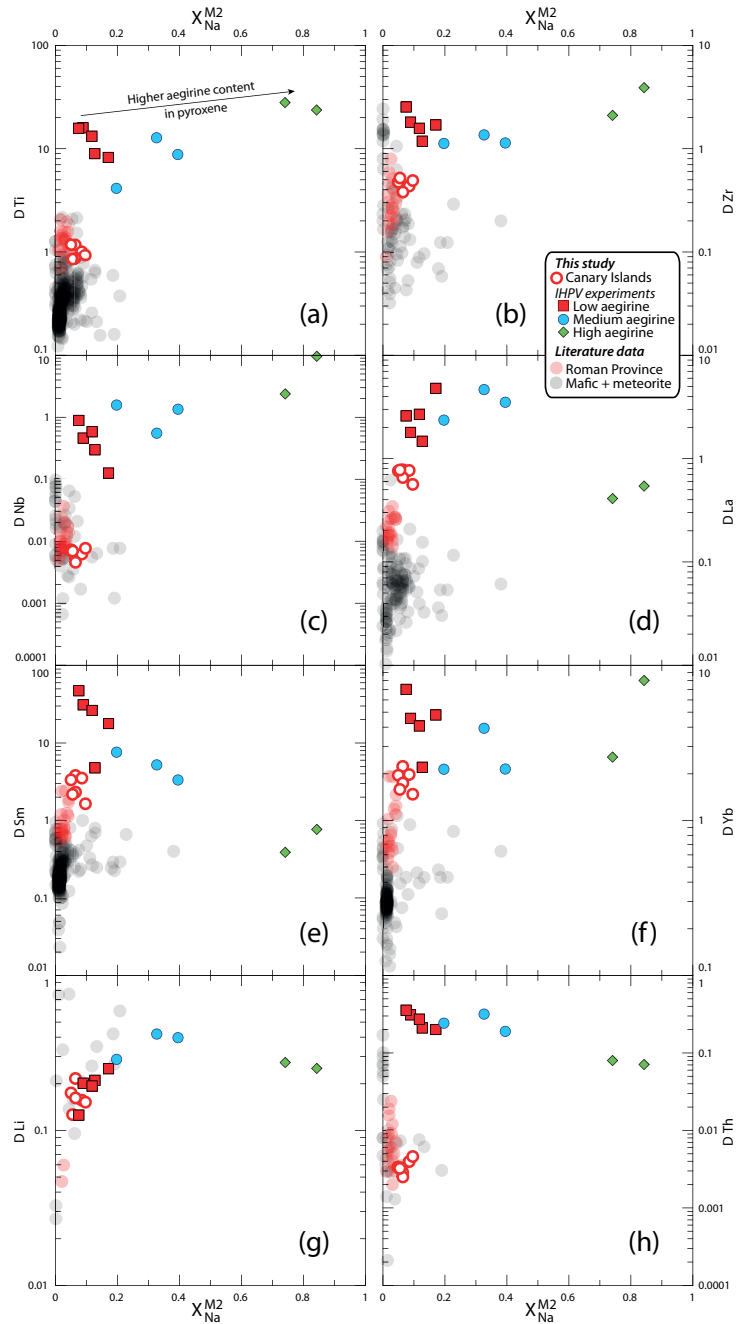


Figure S6: Element partitioning coefficients for HFSE (Ti, Zr, Nb), REE (La, Sm, Yb) and TE (Li, Th) vs.  $X_{Na}^{M2}$ . Literature values ( $n = 411$ ), including those from the Italian volcanoes, are from the compilation of Bédard (2014) and (Mollo et al., 2016).

<sup>1493</sup> **8. Electronic appendices**

xlsx

Table S1: Electronic appendix (.xlsx file) containing experiment starting glass compositions, experiment run conditions, mineral abundances in experimental charges, compositions of reference materials used for EPMA and LA-ICP analyses, major-element concentrations for experiment glasses and clinopyroxene, partition coefficients and fitted lattice-strain parameters.

kml

Table S2: Electronic appendix (.kml file) containing field locations for the Canary Islands samples.

kml

Table S3: Electronic appendix (.xlsx file) containing electron-microprobe transects across experiment clinopyroxene for Ce, Mg and Fe. The data indicate that  $D_{Ce}^{px/melt}$  values determined from our experiments are overestimates, but only by up to 25%. Sector zoning in the clinopyroxene appears to have a larger impact on apparent Ce partitioning behaviour than growth zoning.

pdf

Table S4: Electronic appendix (.pdf file) containing multiple linear regression reports from the stepwise fitting of 3+ cation lattice-strain parameters for the predictive model for element-partitioning (39 pages).

xlsx

Table S5: Electronic appendix (.xlsx file) containing a numerical model for prediction of clinopyroxene/melt element-partitioning coefficients for ions of 3+ valence. Required input data are major-element oxide compositions for clinopyroxene, pressure and temperature. The model for the M2 site is calibrated for application to systems of basaltic to peralkaline phonolite composition. The model for the M1 site is calibrated for use on alkaline to weakly peralkaline systems where the aegirine mol% in clinopyroxene does not exceed 50.